Ensemble Variability in Rainfall Forecasts of Hurricane Irene (2011)

MOLLY B. SMITH,[a] RYAN D. TORN, AND KRISTEN L. CORBOSIERO

University at Albany, State University of New York, Albany, New York

PHILIP PEGION

CIRES, University of Colorado Boulder, and NOAA/Physical Sciences Laboratory, Boulder, Colorado

ABSTRACT

Tropical cyclones (TCs) moving into the midlatitudes can produce extreme precipitation, as was the case with Hurricane Irene (2011). Despite the high-impact nature of these events, relatively few studies have explored the sensitivity of TC precipitation forecasts to model initial conditions. Here, the physical processes that modulate precipitation forecasts over the Northeast United States during Irene are investigated using an 80-member 0.5° Global Forecasting System (GFS) ensemble. The members that forecast the highest total precipitation over the Catskill Mountains in New York (i.e., wet members) are compared with the members that predicted the least precipitation (i.e., dry members). Results indicate that the amount of rainfall is tied to storm track, with the wetter members forecast to move farther west than the dry members. This variability in storm track appears to be associated with variability in analyzed upper-tropospheric potential vorticity (PV), such that the wetter members feature greater cyclonic PV southwest of Irene when Irene is off the Carolina coast. By contrast, the wetter members of a 3-km Weather Research and Forecasting (WRF) Model ensemble, initialized from the same GFS ensemble forecasts, show little sensitivity to track. Instead, the wetter members are characterized by stronger lower-tropospheric winds perpendicular to the eastern face of the Catskills, allowing maximum upslope forcing and horizontal moisture flux convergence during the period of heaviest rainfall. The drier members, on the other hand, have the greatest quasigeostrophic forcing for ascent, implying that the members' differences in mesoscale topographic forcing are the dominant influence on rainfall rate.

1. Introduction

As tropical cyclones (TCs) move from the tropics into the midlatitudes, they often interact with synoptic-scale weather systems, which can yield extensive regions of heavy precipitation (e.g., DiMego and Bosart 1982; Atallah et al. 2007) and widespread, devastating flood events. These flood events are often enhanced by the presence of strong water vapor transport, as terrain interactions disrupt the structure of the TCs' rainbands, causing moisture availability to become the dominant control of rainfall amount (Chen et al. 2010).

The amount of water vapor in poleward-moving TCs can be affected by the process of extratropical transition

(ET; Hart and Evans 2001). ET occurs when a decaying TC acquires baroclinic characteristics and evolves into a cold-core extratropical cyclone (Jones et al. 2003; Evans et al. 2017). At the onset of ET, the TC moves into a baroclinic zone (Klein et al. 2000), placing it near a supply of cold, dry air to its northwest (in the Northern Hemisphere). As the TC proceeds into the baroclinic zone, its cyclonic circulation, coupled with cold air to the north and warm air to the south, gives rise to substantial warm-air advection (WAA) to its east. The WAA is associated with rising air and poleward moisture transport, similar to a warm conveyor belt in an extratropical cyclone (Eckhardt et al. 2004). This transport increases precipitation rates in the region of maximum baroclinicity (Bosart and Dean 1991) to the northeast of the storm center (Atallah and Bosart 2003), where frontogenesis (and quasigeostrophic forcing for ascent) occurs. Cold-air advection (CAA), meanwhile, entrains dry air to the west, which reduces convection in

---

[a] Current affiliation: CIRES, University of Colorado Boulder, and NOAA/Global Systems Laboratory, Boulder, Colorado.

Corresponding author: Molly B. Smith, molly.b.smith@noaa.gov

the storm core, causing the eyewall to dissipate. The net effect of ET on a TC's rainfall patterns, therefore, is to shift the heaviest precipitation outside of the storm core, toward the region of maximum baroclinicity.

One of the reasons that TCs undergo the aforementioned transition is through interactions with midlatitude troughs, which also help steer the TC poleward (e.g., Wu et al. 2007; Torn et al. 2018). As troughs deepen into the midlatitudes and subtropics, they bring colder, higher-potential-vorticity (PV) air equatorward (Hoskins et al. 1985). High-PV perturbations in the atmosphere are associated with cyclonic winds (Davis 1992), so the introduction of a high-PV trough into the vicinity of a TC can substantially alter the environmental steering flow acting upon that cyclone (e.g., Galarneau and Davis 2013). In the case of an upstream trough in the Northern Hemisphere (located to the west of a TC), cyclonic circulation results in variations of southerly steering flow (i.e., southwesterly to southeasterly) depending on the shape of the trough, which in turn can yield differences in the location of heavy rainfall.

In the United States, TC–trough interactions have been responsible for very large precipitation totals. In 1972, Hurricane Agnes interacted with a strong negatively tilted trough over the Great Lakes, placing it in southeasterly environmental steering flow and turning it northwestward into upstate New York and Pennsylvania, where it was associated with widespread rainfall totals of 200–400 mm (DiMego and Bosart 1982). Hurricane Floyd (1999) made landfall in the mid-Atlantic region before turning northward, again due to its interactions with a deep trough situated over the eastern United States (Atallah and Bosart 2003), and deposited flooding rains from North Carolina up through New England. Hurricane Irene (2011) followed a remarkably similar track to Floyd (although it moved slightly farther inland), leading to flooding in many of the same locations (Avila and Cangialosi 2011).

Once the environmental steering flow brings a TC close to land, topography and mesoscale processes play a large role in determining the distribution of precipitation (Chen et al. 2010). The upslope flow generated by a TC's winds blowing orthogonally to a topography gradient provides ascent to produce locally elevated rainfall totals (e.g., Lin et al. 2001, 2011). Wu et al. (2002) performed a modeling study on Typhoon Herb (1996), which brought 1736 mm of rain to Mt. A-Li in Taiwan. In that study, model simulations that employed high-resolution topography for Taiwan's Central Mountain Range produced rainfall totals similar to those observed, while simulations without detailed topography produced hundreds of millimeters less, showing that accurate depictions of mesoscale TC–terrain interactions can greatly enhance precipitation accumulations in models.

In addition to topographical forcings, mesoscale vortices (Harr and Elsberry 1996) and frontogenetic regions (Gao et al. 2009) can form within the larger TC circulation, leading to increased ascent and higher rainfall amounts (Wu and Kuo 1999). Colle (2003) found Hurricane Floyd (1999)'s highest mid-Atlantic rainfall totals occurred along a frontogenetic band that formed as Floyd underwent ET, with terrain playing a small role.

It is necessary to consider both synoptic and mesoscale dynamics when creating accurate precipitation predictions for TCs. In this regard, numerical weather prediction models provide invaluable guidance. Global models, such as the National Centers for Environmental Prediction's (NCEP's) Global Forecast System (GFS) and the European Centre for Medium-Range Weather Forecasts (ECMWF)'s model, simulate the atmosphere over the entire globe, incorporating spherical harmonic solutions for dynamical equations and parameterizing smaller-scale processes (Krishnamurti 1995). Regional models, such as the Weather Research and Forecasting (WRF) Model, have more localized domains, can use higher resolution, and are more easily customizable (Michalakes et al. 2001; Benjamin et al. 2016). Both types of models assimilate observational data in an attempt to improve accuracy (Rabier 2005), but a single, deterministic model simulation is prone to increasing error with time, due to the chaotic and/or unstable nature of the atmosphere (Lorenz 1963). This error amplification is especially apparent when ET is involved, as current weather models sometimes have difficulty accurately simulating the dynamics of ET (Davis et al. 2008), both in terms of TC–jet interactions (Keller et al. 2019), and in terms of the accurate modeling of convection (Bassill 2015). Many authors have advocated the use of probabilistic forecasts as a way to account for errors arising from initial condition and modeling inaccuracies (e.g., Epstein 1969; Gleeson 1970; Karstens et al. 2015), and ensembles are a relatively computationally efficient manner to generate these probabilistic forecasts (e.g., Krishnamurti et al. 2000).

This study will examine the effects that initial condition uncertainty can have on rainfall forecasts using Hurricane Irene (2011) as a case study. Irene directly caused 41 deaths and $15.8 billion (U.S. dollars) in damages, with three towns in the Catskills deemed uninhabitable due to flooding from heavy precipitation (Avila and Cangialosi 2011). Storms such as Irene emphasize the importance of accurate forecasts in preparing for, and mitigating, the negative effects of TC-enhanced rainfall on communities. Track and intensity forecasts for flood-inducing TCs have improved substantially in recent years (Yamaguchi et al. 2015), largely due to advances in numerical weather prediction, although models still retain some biases and inaccuracies (e.g., Davis et al. 2016).
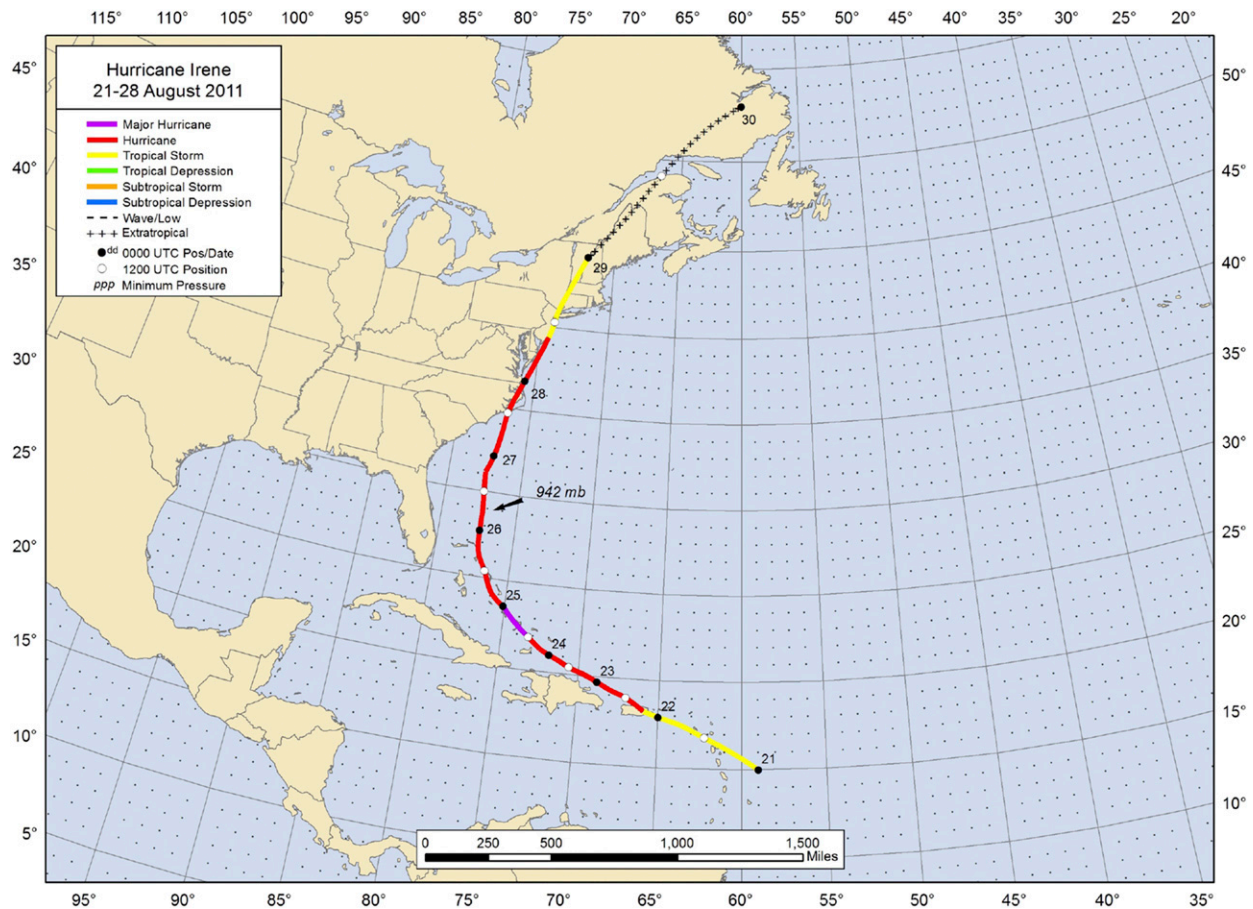
FIG. 1. Track and intensity of Hurricane Irene from 21 to 29 Aug 2011. (Source: NOAA NHC.)

The goal of this work is to understand what modulates precipitation forecasts over the northeastern United States during Irene by examining the differences between members of an ensemble forecast that predict higher versus lower precipitation totals in a certain location. Even though the members all use the same physics, small differences in the initial location and intensity of features in the vicinity of Irene can be magnified by the process of ET, eventually producing much different forecasts.

The synoptic history of Hurricane Irene is provided in section 2, and the data and methods in section 3. Section 4 analyzes the results of a synoptic-scale GFS ensemble, while section 5 does the same for a mesoscale WRF ensemble. Section 6 presents a summary and conclusions.

2. Synoptic history of Hurricane Irene

Irene formed from a tropical wave that moved off the coast of Africa on 15 August 2011. It was named as a tropical storm late on 20 August while located to the east of Martinique, and began to move west-northwest through the Caribbean Sea. The storm reached hurricane strength on 22 August, while located just off the east coast of Puerto Rico, causing extensive flood damage there before moving northwestward and strengthening to a category 3 hurricane. On 24 August, Irene turned northward toward the Bahamas and the U.S. East Coast. After passing over the Bahamas as a category 2 hurricane, Irene made landfall near Cape Lookout, North Carolina, at 1200 UTC 27 August as a category 1 hurricane, before reemerging over the Atlantic and continuing on a northward track (Fig. 1). Irene made its final landfall as a tropical storm with 55-kt ($1\,kt \approx 0.51\,m\,s^{-1}$) winds shortly after 1200 UTC 28 August, just east of New York City, and was declared extratropical at 0000 UTC 29 August (Avila and Cangialosi 2011).

As Irene moved north from the tropics to the midlatitudes, the storm's motion was strongly influenced by two separate troughs situated over the continental United States. On 24 August, when Irene tracked over the southern Bahamas, it began to interact with a weak, cyclonic, upper-level PV perturbation over the southeastern
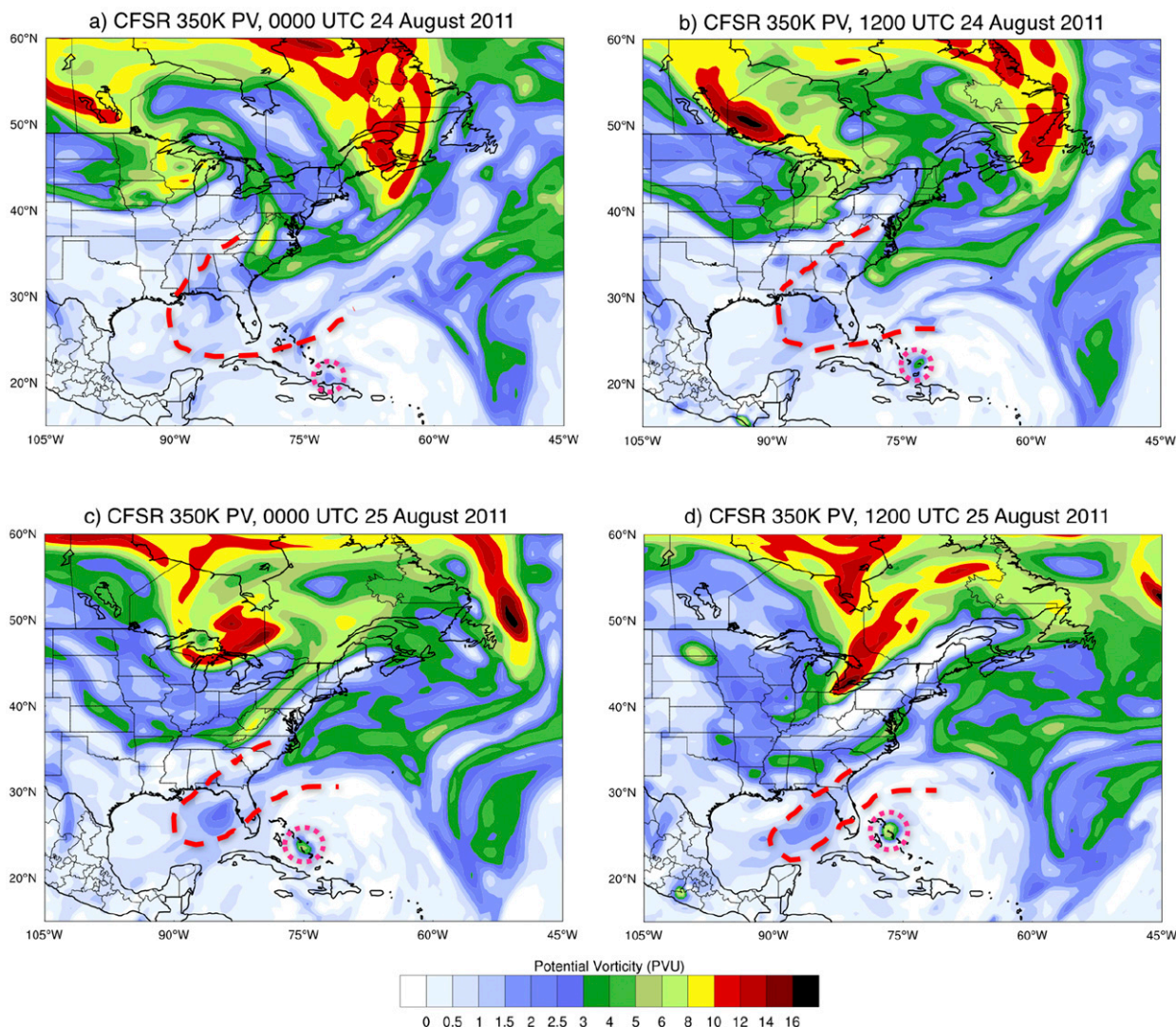
FIG. 2. Climate Forecast System Reanalysis (CFSR) 350-K PV at (a) 0000 UTC 24 Aug, (b) 1200 UTC 24 Aug, (c) 0000 UTC 25 Aug, and (d) 1200 UTC 25 Aug. Hurricane Irene is outlined in pink and the first upstream trough is outlined in red.

United States and Gulf of Mexico (Fig. 2a). Because this trough was situated to the west of Irene, its cyclonic circulation placed the TC in a region of southerly flow, turning Irene north toward the United States (Figs. 2b–d). By the time Irene reached the Carolinas, a second, stronger trough was present over the central and eastern United State, once again placing the TC in a region of southerly steering flow, sending the storm north toward New York and the northeastern United States (Figs. 3a–e).

Like other TCs that interact with upstream troughs, Irene caused substantial flooding and damage across the Northeast United States. As it moved inland, it deposited widespread rainfall totals of 100–170 mm, with locally higher amounts. The Catskill region of New York (Fig. 4), in particular, received very large amounts of precipitation, with some locations seeing up to 300 mm of rain in less than 24 h (Avila and Cangialosi 2011).

3. Data and methods

a. GFS 0.5° model description

To investigate precipitation variability between members, an 80-member ensemble of the 2014 experimental version of the GFS was initialized at 0000 UTC 27 August 2011 (when Hurricane Irene was off the coast of North Carolina; Fig. 3a) and run through 0000 UTC 29 August 2011 (when Irene was declared extratropical over New England; Fig. 3e). This 80-member ensemble was initialized by taking the ensemble perturbations from the GFS ensemble Kalman filter
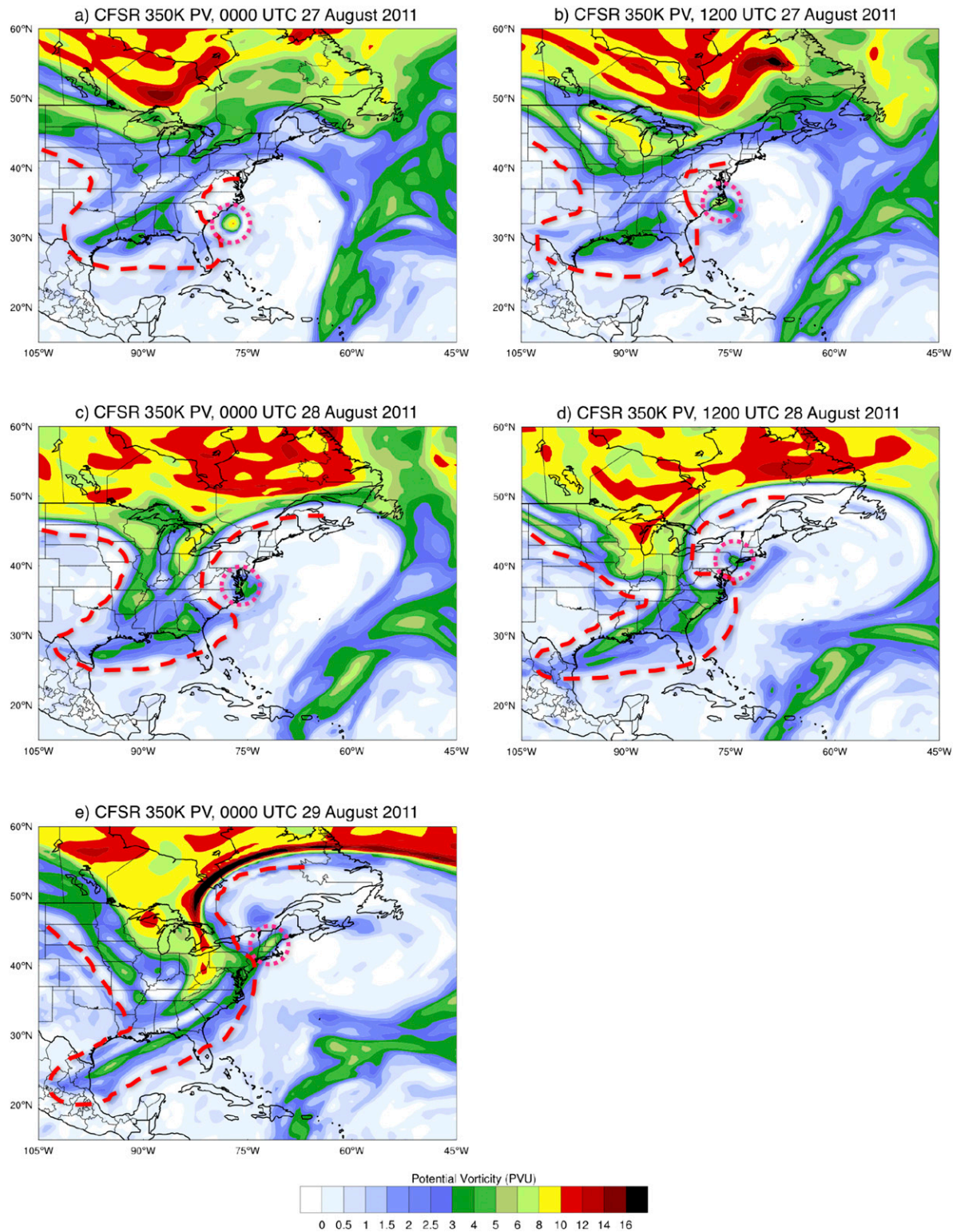
FIG. 3. CFSR 350-K PV at (a) 0000 UTC 27 Aug, (b) 1200 UTC 27 Aug, (c) 0000 UTC 28 Aug, (d) 1200 UTC 28 Aug, and (e) 0000 UTC 29 Aug. Hurricane Irene is outlined in pink and the second upstream trough is outlined in red.
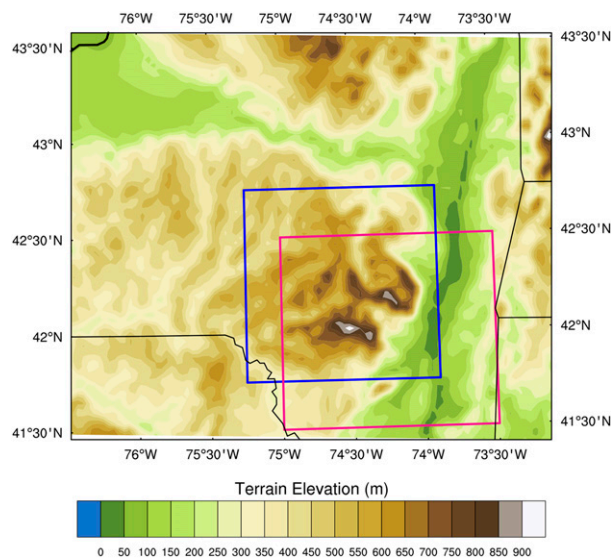
FIG. 4. Southeastern New York terrain height (as depicted in the 3-km WRF) and defined Catskills bounds for the GFS (pink box) and 3-km WRF (blue box) analyses.

(EnKF; Whitaker and Hamill 2002) analysis and re-centering them such that the ensemble mean of the 80 members is the high-resolution analysis (~27 km) of the control forecast. These forecasts were output with 0.5° spatial resolution and 3-hourly temporal resolution, and examined in terms of differences in simulated rainfall over the Catskills (defined here as the area encompassed by 41.5°–42.5°N, 73.5°–75°W; Fig. 4).

b. WRF 3-km model description

Although the GFS is a good synoptic-scale model, it can have difficulty producing accurate precipitation forecasts over regions of complex terrain (e.g., Carpenter et al. 2004). The relatively low-resolution terrain in this model does not accurately resolve sharp topographic gradients or individual peaks and valleys and, thus, does not accurately reflect the mesoscale forcings or hydrology of complex areas. To examine the role that terrain resolution played in the evolution of precipitation in Hurricane Irene, the 0.5° GFS ensemble output was used to provide initial and boundary conditions to produce a 3-km WRF ensemble forecast for the same time period, also initialized at 0000 UTC 27 August 2011. This ensemble was produced with WRF version 3.6, with physics comparable to those employed in the High-Resolution Rapid Refresh model (Benjamin et al. 2016): Thompson microphysics (Thompson et al. 2004), the Rapid Radiative Transfer Model for Global Climate Models longwave and shortwave radiation (Mlawer et al. 1997), the Mellor–Yamada–Nakanishi–Niino planetary boundary layer and surface scheme (Nakanishi and Niino 2009), the Rapid

Update Cycle land surface model (Benjamin et al. 2004), and the Kain–Fritsch cumulus parameterization (Kain 2004). This model configuration had an outer 15-km nest over the eastern United States and western Atlantic (25°–50°N, 60°–95°W), and an inner 3-km nest spanning the eastern United States from Michigan to Maine (29°–46°N, 68°–87°W), chosen to be large enough to encompass the track of Hurricane Irene and the surrounding area for the entire 48 h forecast. The 3-km grid was of sufficiently high resolution that it was not necessary to use a cumulus scheme.

4. GFS ensemble rainfall variability

As discussed in section 1, this work uses Hurricane Irene as a case study to examine ensemble variability in rainfall forecasts for the Catskill region of New York. Sets of the wettest and the driest GFS ensemble members (in terms of Catskills precipitation) are, therefore, compared to deduce the physical and dynamical processes responsible for their differences in forecast precipitation.

a. General overview of ensemble member rainfall characteristics

The performance of the ensemble as a whole was assessed by comparing the 48-h ensemble mean and standard deviation of precipitation to Stage IV observations, obtained from the Earth Observing Laboratory (Du 2011). Overall, the GFS ensemble mean did well at predicting the spatial extent of Irene's rainfall. Both the ensemble mean and the observations feature a rain swath about 5° of longitude wide extending from North Carolina up through New England (Figs. 5a,b). The highest rain totals were also correctly located over the mid-Atlantic and Carolina coastlines. The ensemble mean underpredicted the actual amount of rainfall received nearly everywhere over land, however, and did not reproduce the greater than 254-mm accumulations seen over North Carolina, Delaware, or the Catskill region of New York (Fig. 5c). These differences are to be expected, as the ensemble mean damps out any local maxima seen in individual members, resulting in a smooth, lower-magnitude distribution of values. The high forecast standard deviation (Fig. 5d) seen over Virginia and North Carolina, as well as over the Catskills, suggests that some members produced locally higher totals, and an examination of individual ensemble members showed that many of these simulations did produce maxima above 254 mm, but in differing locations (not shown).

The ensemble mean forecast (Fig. 5b) displays a sharp gradient on the western edge of the precipitation swath, which, when paired with the variation in storm position between individual ensemble members, could explain
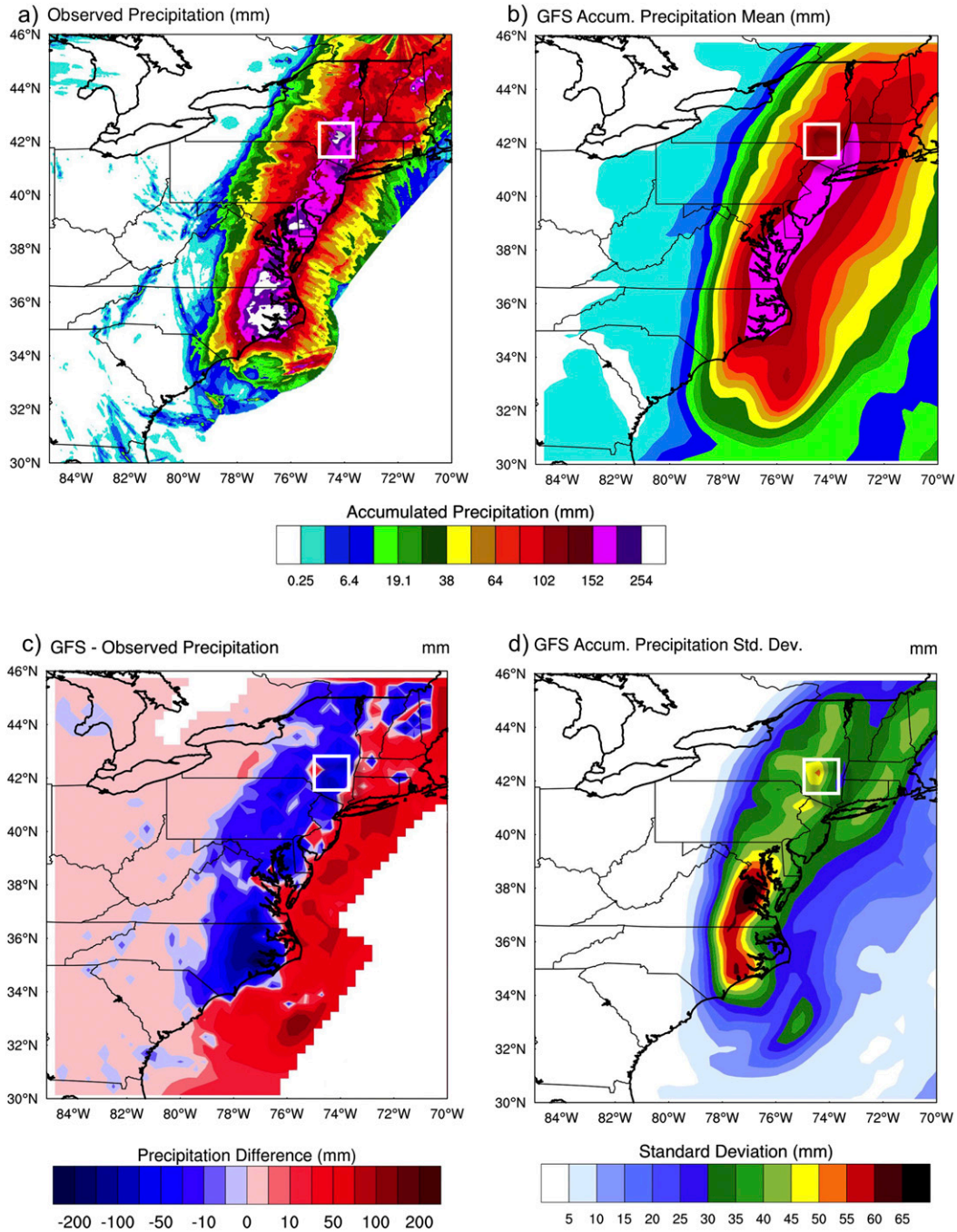
FIG. 5. (a) Observed accumulated precipitation (mm), (b) GFS ensemble mean total accumulated precipitation (mm), (c) difference between the ensemble mean and observed accumulated precipitation (mm), and (d) GFS ensemble standard deviation (mm) from 27 to 29 Aug 2011. The Catskills domain is indicated by the white box.

some of the precipitation variability seen in the ensemble. If individual ensemble members tracked Irene to the east or west of the mean storm path, thereby shifting the position of the rain swath, locations along that western edge (including the Catskills) could receive substantially different rainfall totals from one simulation to the next.

To test this hypothesis, the mean predicted storm track for each ensemble member was derived by finding the latitude and longitude of the minimum value in the mean sea level pressure field at 3-hourly intervals. When the total 48-h precipitation received by the Catskills was compared to the average storm track longitude for each ensemble
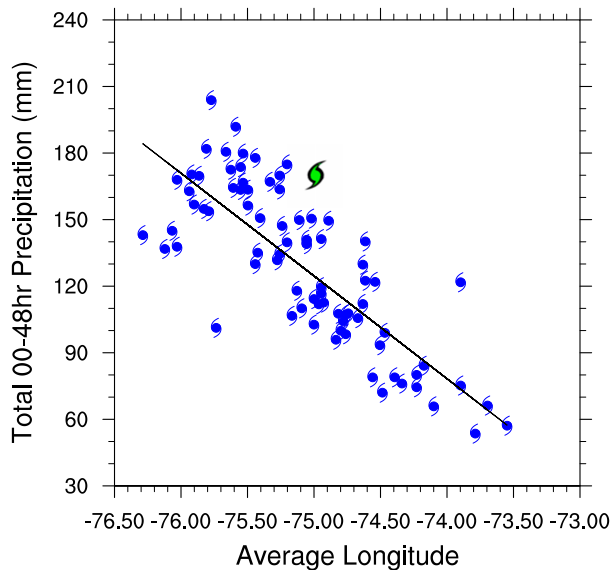
FIG. 6. Accumulated 27–29 Aug 2011 Catskills precipitation (mm) as a function of Irene's average storm track longitude (°E) over the same time period for each GFS ensemble member (blue). Irene's observed position and precipitation is indicated in green.

member (Fig. 6), the data show a strongly linear relationship between these two variables ($r = 0.77$), with higher precipitation for members where Irene moves farther west. The linearity suggests that storm position was a dominant factor controlling Catskills rainfall amount. Furthermore, the best track (Landsea and Franklin 2013) value was about 0.3° of longitude to the west of the ensemble mean track at final landfall, suggesting that the westward-tracking members provided a more accurate forecast of Irene's motion than the eastward-tracking ones.

b. Comparison of the 10 wettest and 10 driest ensemble members

As discussed in section 4a, the wet and dry members have different forecast tracks; therefore, it is important to diagnose what factors modulated Irene's simulated motion. TC motion can be influenced by the timing and orientation of upstream features (Carr and Elsberry 2000), so a working hypothesis for the differences observed in the ensemble is that differences in track between the wet and dry members are due to differences in the evolution of Irene and these upstream features. This hypothesis was tested by taking the normalized difference between composite fields from the 10 wettest ensemble members and the 10 driest. The normalized difference for each field in question is computed with the formula

$$\Delta x_i = \frac{\overline{x}_i^{\text{wet}} - \overline{x}_i^{\text{dry}}}{\sigma_{x_i}},$$

where $\overline{x}_i^{\text{wet}}$ represents the mean of the ith field for the wet members, $\overline{x}_i^{\text{dry}}$ represents the mean of the ith field for the dry members, and σ_{x_i} is the ensemble standard deviation of the ith field (Torn et al. 2015). Normalizing by the standard deviation allows disparate fields and times to be compared to one another, even if the fields have different intrinsic variability and/or units. Some fields (indicated in the text) were smoothed using a 200-km area average filter, meaning that each grid point of the 2D field displayed in those figures represents the average value of the 200-km radius area immediately surrounding it. Statistical significance was computed at $\alpha = 0.05$ using a Student's t-test (Ruxton 2006). If the above hypothesis is true, significant positional differences should be observed both in Irene and in upstream features.

When composite difference plots of 200-km area-averaged circulation at 300 hPa (Fig. 7) are examined, the positional differences between synoptic-scale features become increasingly apparent with time (300 hPa was selected to display the strong, upper-level circulations associated with the TC and the midlatitude jet). Although there are small differences between the two composites at 0 h, (Fig. 7a), statistically significant differences appear around Irene by 6 h (Fig. 7b), as evidenced by the $\pm$ 0.8 difference dipole centered on Irene. The positive values to Irene's west indicate that the wetter members positioned Irene's circulation west of the ensemble mean, while the negative values to its east show that the drier members positioned the storm east of the ensemble mean. This positional difference grew in magnitude through 18 h (Fig. 7c) and 36 h (Fig. 7d), when Irene made landfall in New York.

In addition to the differences associated with Irene's position, the wet and dry members are characterized by differences in the placement of the upstream trough located over the Great Lakes. At 6 h, the positive circulation connected to the leading edge of the trough had progressed slightly farther east in the drier members (as evidenced by the -0.8 differences in place over Pennsylvania and Virginia), although this perturbation is not statistically significant. By 18 h, the upstream trough in the drier members had progressed significantly farther to the east (as evidenced by statistically significant -1.6 differences over western New York and Pennsylvania), than the trough in the wetter members, which remained over the Great Lakes. When Irene made landfall at 36 h, the positional differences in the trough were especially pronounced over the eastern Great Lakes, and western New York and Pennsylvania, with differences greater than $\pm$ 2. The fact that Irene developed statistically significant positional differences before the upstream trough suggests that the majority of the precipitation forecast variability originated in the vicinity of the TC,
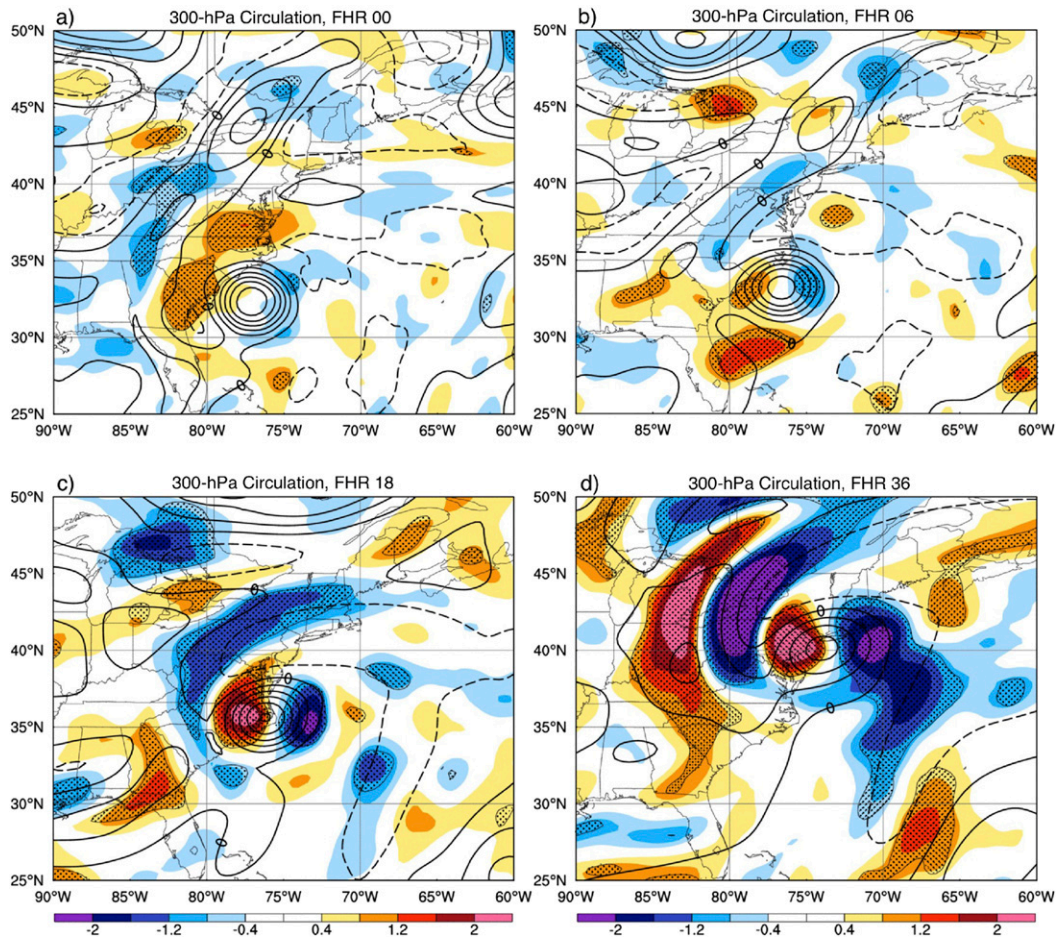
FIG. 7. The 300-hPa circulation differences between the 10 wettest and 10 driest members at (a) 0, (b) 6, (c) 18, and (d) 36 h. In this plot, contours represent the ensemble mean circulation (spaced by $1 \times 10^{-5}\,\mathrm{s}^{-1}$), color shading represents the standardized difference between the wet member composite field and the dry member composite field, and stippling represents regions of statistical significance.

rather than within the midlatitudes. This scenario suggests the hypothesis that Irene moved farther west during the first 12–18 h of the wetter simulations, possibly due to a slightly stronger anomalous easterly component of the steering flow, and created more blocking to the northwest, which could slow the approaching trough. This slower trough would have allowed Irene to maintain a more northward heading into eastern New York, rather than being accelerated to the northeast, which in turn placed the maximum rainfall rates over the Catskills.

To test this hypothesis, composite difference plots of 250–850-hPa zonal steering flow were examined (Fig. 8). Zonal steering flow was calculated by removing the irrotational and nondivergent wind vectors from the total wind within a 3° radius of the TC following Galarneau and Davis (2013). At 0 h, the wet members placed Irene in a broad region of statistically significant, anomalous

easterly steering flow, as evidenced by the −1.2 standardized zonal flow anomalies maximized to the northeast of Irene (Fig. 8a). By 6 h, the magnitude of the difference between the wetter and the drier members increased, with Irene situated at the center of a strong easterly perturbation wind (represented by difference values from −1.6 to −2; Fig. 8b). By 18 h, the easterly perturbation winds increased in amplitude and grew in area (Fig. 8c), persisting through the time of Irene's landfall (Fig. 8d). Thus, from the time of model initialization, the wetter members possessed the necessary synoptic setup to steer Irene closer to the approaching trough than the dry members.

Torn et al. (2015) performed a similar verification of GFS ensemble forecasts of Hurricane Sandy (2012), and also found that ensemble members that produced westward tracks were characterized by easterly perturbations in the steering flow surrounding the storm. In Sandy,
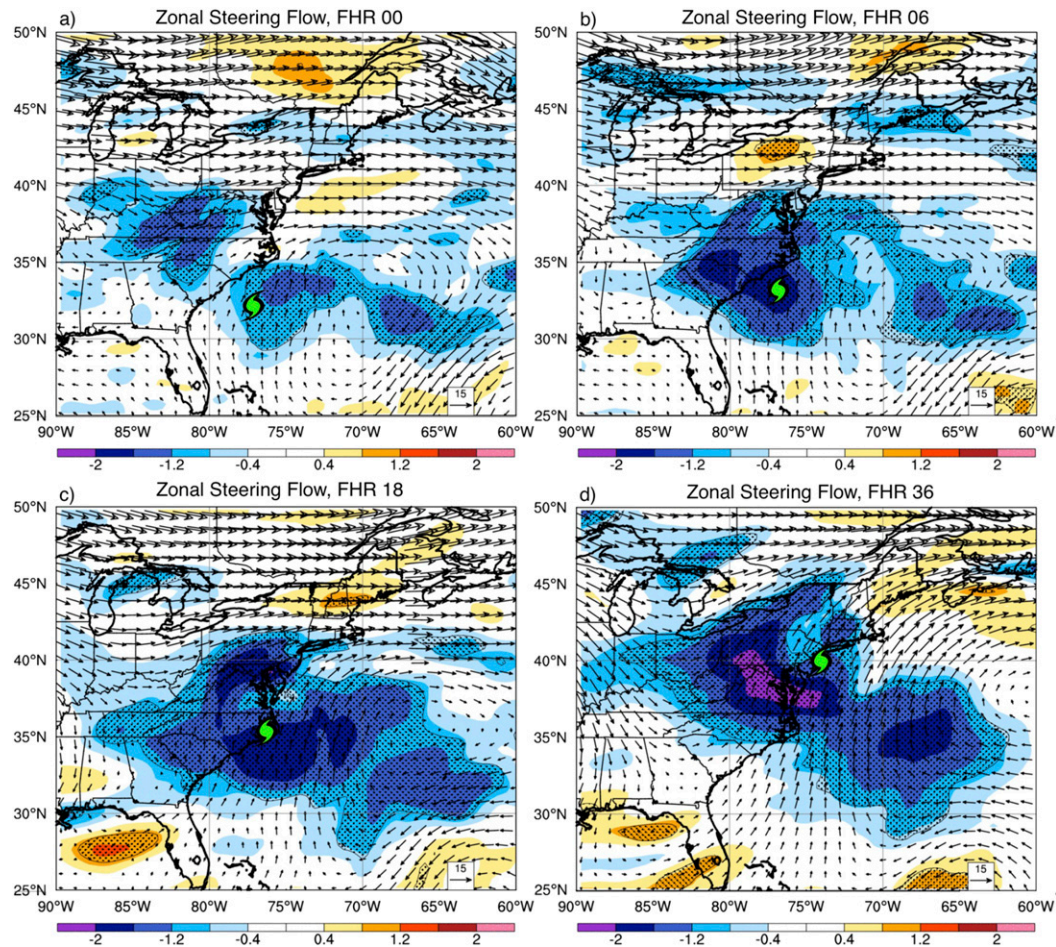
FIG. 8. As in Fig. 7, but for 250–850-hPa zonal steering flow (m s^{-1}). The green cyclone marker represents the position of Irene at each time.

the easterly perturbations were determined to have been the result of a negative-PV anomaly associated with an anticyclone poleward of Sandy. The clockwise flow around the negative-PV anomaly resulted in increased anomalous easterly flow to its south, steering Sandy farther west.

To test whether a similar PV anomaly was responsible for steering Irene, composite differences were computed for the 350-K PV field (Fig. 9). As with the 300-hPa circulation, the 350-K PV layer was chosen to provide a good depiction of upper-tropospheric features. At 0 h (Fig. 9a), the wetter members featured a positive difference along the region of positive PV to the southwest of Irene, just off the coast of northeastern Florida (at approximately 30°N, 80°W). The cyclonic flow associated with this positive PV anomaly should be associated with an easterly steering flow perturbation in the vicinity of Irene (Fig. 8a), yielding a perturbation westward motion. The cyclonic PV anomaly persisted through 6 h (Fig. 9b), maintaining the increased anomalous easterly steering flow in the wet members (Fig. 8b). By 18 h (Fig. 9c), the

initial PV perturbation was no longer present; however, a significant difference had developed between the wet and dry members placement of both the TC and the upstream trough, as evidenced by the <-2 perturbations over the Appalachians, indicating that the high-PV trough had not yet progressed to that region for the wet members. The anticyclonic flow anomalies associated with this PV difference placed Irene once again in a region with stronger easterly steering flow (Fig. 8c), which persisted through the storm's landfall at 36 h (Fig. 9d).

As the wetter members steered Irene farther west, closer to the midlatitude trough, there was a greater likelihood of interaction between the two features. One way that a TC can interact with an upstream trough is by slowing the approach of the trough via PV advection from the TC's divergent outflow (e.g., Harr et al. 2008; Riemer et al. 2008; Archambault et al. 2015). Figure 10 applies this concept to Irene by showing a composite difference plot of 250-hPa irrotational flow at 6, 9, 12, and 15 h. These times represent the period during which the position differences in Irene
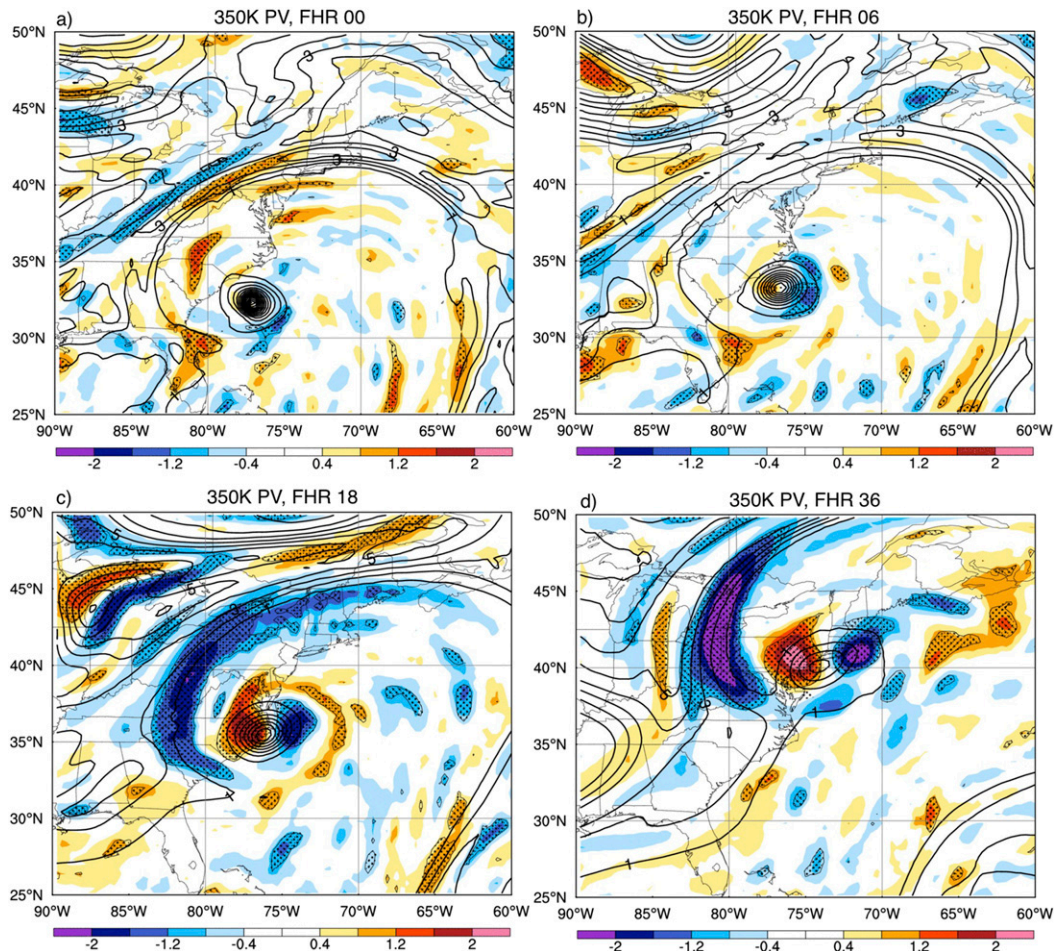
FIG. 9. As in Fig. 7, but for 350-K PV [contours spaced by 1 PVU (1 PVU $= 10^{-6}$ K kg^{-1} m^2 s^{-1})].

and the upstream trough were developing. The ensemble mean upper-level outflow was strongly divergent throughout this period, represented in the ensemble mean as a starburst pattern of outward-pointing vectors radiating from the TC's center. At 6 h, an easterly wind perturbation began to form along the leading edge of the upstream trough (represented by the negative differences over the Appalachians), indicating that the wetter members were beginning to have higher magnitude irrotational wind directed up the PV gradient toward the trough (Fig. 10a). As time progressed, this easterly wind perturbation increased in magnitude, becoming statistically significant (Figs. 10b–d) and providing a mechanism for the wetter members to advect low-PV air into the approaching trough, slowing its progression.

These analyses show that the wetter members are the ones in which easterly steering flow perturbations started Irene on a more westward course, bringing its divergent outflow in closer proximity to the upstream trough in the midlatitude flow. The outflow then advected more low-PV air poleward and westward, slowing the forward progression of the high-PV trough. This interaction set up a two-stage process between Irene and the midlatitude waveguide, wherein Irene advected low-PV air poleward and westward, slowing the trough, which allowed Irene to track even farther west, further advecting low-PV air and slowing the trough further. This interaction was largely absent in the eastward-tracking members, which never got close enough to the trough to effectively slow its progress. Altogether, the information provided in Figs. 8–10 illustrates that the differences in Irene's track were due to differences in the positions of upstream features, which in turn were due to differences in PV and steering flow at analysis.

5. WRF 3-km ensemble rainfall variability

a. General overview of ensemble member rainfall characteristics

One major conclusion of section 4 was that GFS ensemble rainfall variability in the Catskills was mainly
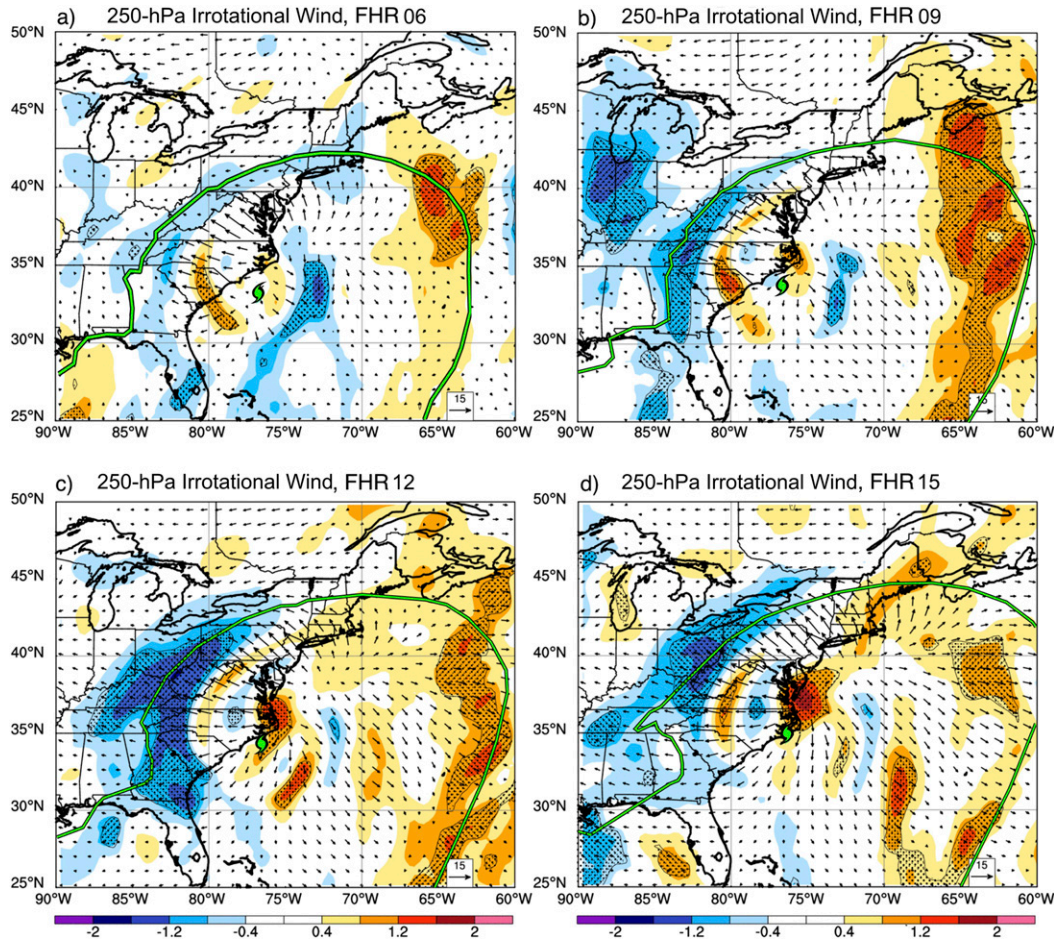
FIG. 10. As in Fig. 7, but for 250-hPa irrotational zonal wind (m s^{-1}) at (a) 6, (b) 9, (c) 12, and (d) 15 h. The green cyclone marker represents the ensemble mean position of Irene, and the green contour denotes the ensemble mean 2-PVU contour on the 350-K surface at this time.

due to Irene's east–west position variability between individual members. A question that must be answered, therefore, is whether position remains the dominant driver of variability when the 3-km WRF's higher-resolution terrain is considered. For this analysis, new boundaries (41.75°–42.75°N, 73.9°–75.25°W) were defined for the Catskills in the WRF 3-km output, to better reflect the actual location of the mountain range in the higher-resolution topography (Fig. 4).

Like in the GFS ensemble members, the 3-km WRF storm tracks do feature several longitudinal degrees of variability (from 73.5° to 76.5°W; Fig. 11). Individual members have roughly the same average storm track longitude in the 3-km WRF ensemble as they do in the GFS ensemble (Fig. 11a), but the 3-km WRF ensemble does not feature a linear relationship between Catskills precipitation and storm track average longitude (Fig. 11b). Members with storm tracks near the center of the longitude distribution (around 75.25°W) have generally higher

precipitation amounts, although precipitation at these longitudes vary by as much as 60 mm.

Because the 3-km WRF ensemble features a more complex relationship between precipitation and storm track than a simple east–west correlation, composite difference plots of the 10 wettest and 10 driest ensemble members were not effective analysis tools for this ensemble. Instead, a different objective clustering of ensemble members based on the precipitation field was employed to address the question of what modulates rainfall variability over the Catskills.

b. Objective clustering

For the objective clustering analysis, the k-means objective clustering algorithm (Hartigan and Wong 1979) was used to group the 80 ensemble members into three clusters (Fig. 12a), based on the distribution of rainfall over the domain 41.5°–43.5°N, 73°–76.5°W at 39 h into the forecast. In this case, the k-means algorithm places each
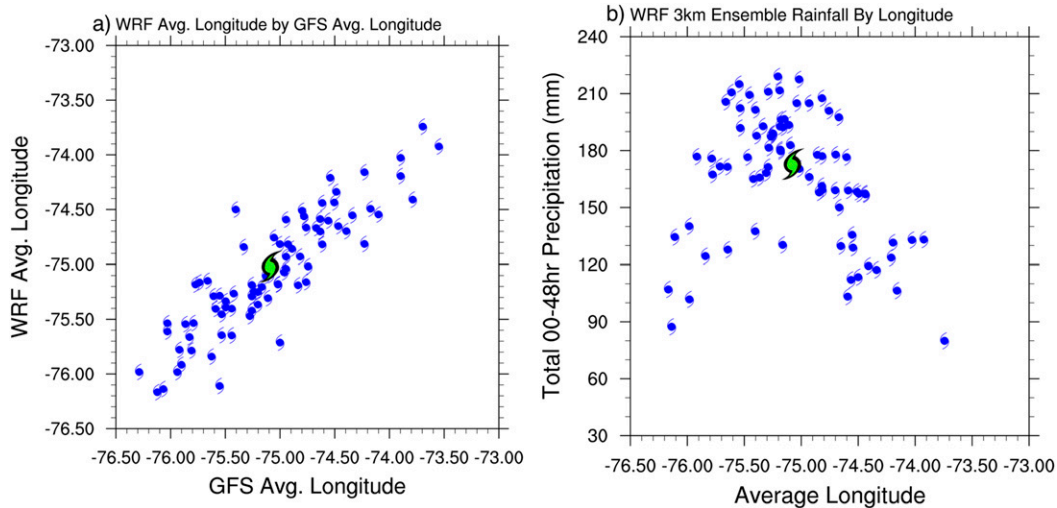
FIG. 11. (a) GFS average storm track longitude (°E) compared to WRF 3-km average storm track longitude for each ensemble member, and (b) WRF 3-km average storm track longitude compared to total Catskills rainfall (mm) for each ensemble member. For both ensembles, storm track longitude is averaged for the time period 0000 UTC 27 Aug–0000 UTC 29 Aug 2011. Irene's observed position and precipitation is indicated in green.

member into the cluster where that member's particular rainfall distribution produces the smallest squared error when compared to the cluster mean precipitation distribution. A duration of 39 h was selected because it featured the highest precipitation rates over the Catskills domain, and members with the greatest rainfall at this time generally produced the greatest total accumulations over the region. This clustering methodology was proven to be robust, as very similar groupings were produced when the members were clustered based on the horizontal distribution of total precipitation, instead of just 39-h precipitation, and when all 80 members were time shifted so that their maximum rainfall rates occurred at the same forecast hour. In addition, using more than three clusters proved to be redundant (not shown), indicating that three is sufficient to accurately portray the variability present in the ensemble. A similar approach was also performed on the GFS ensemble output; however, this approach did not yield any unique insights as horizontal rainfall distribution, and thus cluster designation, is overwhelmingly controlled by Irene's position relative to the Catskills (not shown).

Once the clustering was performed on the WRF ensemble, the first cluster was comprised of members where Irene moved to the center and west of the ensemble swath (Fig. 12b; blue), the second consisted of members with central and easterly tracks (Fig. 12b; red), and the third was a residual cluster, encompassing members that were either too slow or too far from the ensemble mean track to result in significant rainfall over the Catskills (Fig. 12b; green). The western cluster brought the highest rainfall totals to the Catskills, while

the eastern cluster brought reduced, although still substantial, accumulations (Fig. 12c; blue and red lines). The residual cluster brought the least rain, as its members placed the precipitation too far south and east. The remainder of this section will focus on comparisons of the wetter, western cluster and drier, eastern cluster as two scenarios representing simulations where Irene tracked close enough to the Catskills to greatly affect the region, and differences in rainfall rates were driven by differences in model dynamics, rather than differences in proximity to the Catskills. The residual cluster, while technically the driest, was dry because its component simulations never brought Irene particularly close to the Catskills and, thus, it is not as relevant to our analysis.

There are several potential hypotheses that can explain the variability between the wetter and drier clusters, including: 1) wetter members feature greater upslope forcing over the Catskills, 2) wetter members have increased moisture flux convergence over the Catskills, and 3) wetter members position the region of greater quasigeostrophic forcing for ascent over the Catskills. It should be noted that the first two of these hypotheses are related to mesoscale dynamics and terrain effects, and are not entirely independent of one another (as upslope flow in a moist environment will be associated with moisture flux convergence), while the third hypothesis is more closely tied to synoptic-scale dynamics.

Figure 13 tests the first of the three hypotheses by comparing the composite 900-hPa winds and 3-h precipitation rate in relation to terrain for the wetter cluster (Figs. 13a,c) and the drier cluster (Figs. 13b,d) at the time of maximum precipitation over the Catskills. The wetter
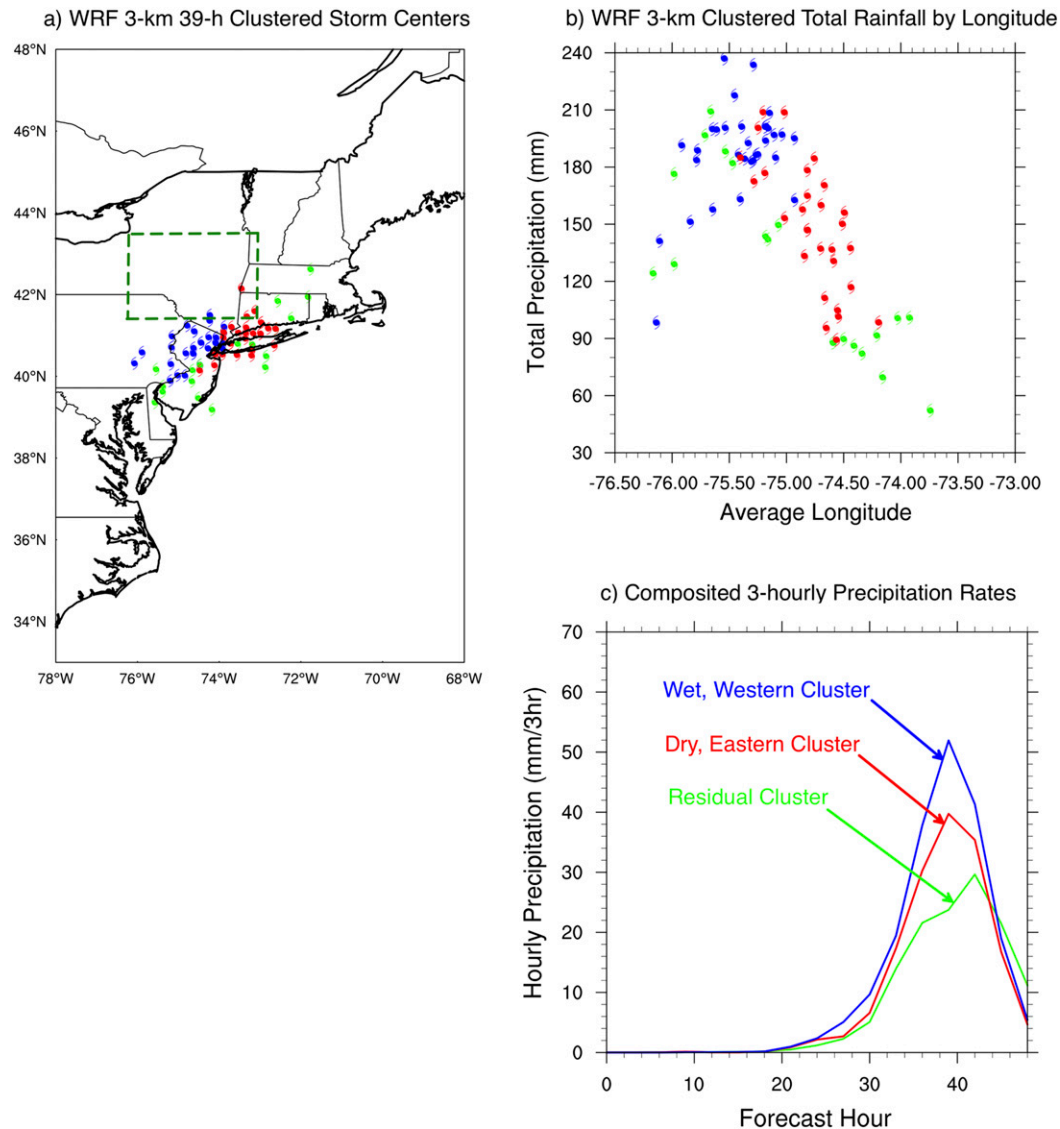
FIG. 12. (a) Storm center positions at 39 h into the simulation sorted into three clusters (represented here by color). Clusters are based on the horizontal distribution of precipitation at this time over the domain outlined in green (41.5°–43.5°N, 73°–76.5°W). (b) As in Fig. 11b, but with each member color coded by cluster, over the domain outlined in green. (c) Composite time series of precipitation rate [mm (3 h)$^{-1}$] over the Catskills for each cluster.

members positioned Irene directly south of the Catskills at this time, with associated easterly low-level winds directed perpendicular to the steep eastern slopes of the Catskills, where the highest rainfall rates were observed. The drier members, on the other hand, positioned Irene to the southeast, resulting in a more northerly flow into southeastern New York (with a wind angle more than 45° different from that of the wet members at 39 h), impacting shallower terrain gradients on the northern side of the Catskills, which in turn would lead to lower vertical velocities. This difference between the two clusters is illustrated in a schematic in Figs. 14a and 14b.

To quantify these differences, an upslope metric, $\mathbf{V}_{10} \cdot \nabla Z_s$ (where $\mathbf{V}_{10}$ is the 10-m horizontal wind vector and ∇Z_s is the gradient of the terrain height; Tang et al. 2016), was used to examine upslope flow over the Catskills. With this metric, it can be seen that the wind setup in the wetter members features strong bands of upslope forcing along the eastern facing slopes of the Catskills (near 42°–42.5°N, 74°–74.5°W; Fig. 15a), coupled with very little downslope forcing anywhere in the mountains. By contrast, the drier members do have strong upslope forcing along the northeastern facing slopes, but also broad areas of downslope forcing
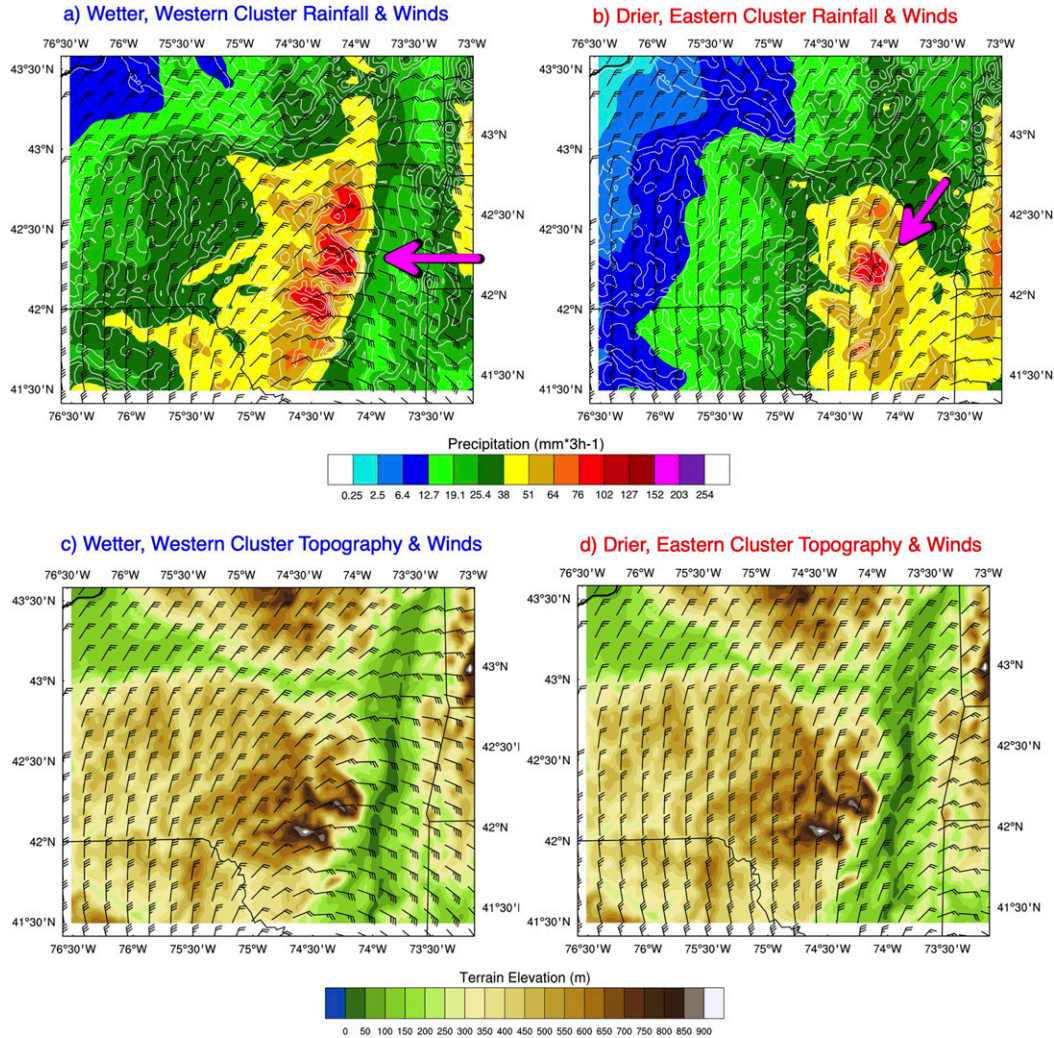
FIG. 13. The 39-h precipitation [shaded; mm $(3\,\mathrm{h})^{-1}$], 900-hPa winds (barbs, where a short tick denotes $5\,\mathrm{m\,s^{-1}}$ and a long tick denotes $10\,\mathrm{m\,s^{-1}}$), and topography (white contours every 100 m) for (a) the wet, western cluster and (b) the dry, eastern cluster. The pink arrow indicates the predominant wind direction into the Catskills. (c),(d) As in (a) and (b), but without the rainfall layer to better illustrate the relationship between the winds and terrain.

throughout the rest of the Catskills (Fig. 15b). This difference is especially noticeable over the southeastern part of the Catskills (near 42°N, 74°15′W), where the wetter members place a strong band of upslope forcing and the drier members have intense downslope. An examination of Fig. 13 reveals that this region had one of the largest differences in precipitation rate between the western and eastern clusters, with the former receiving over 102 mm $(3\,\mathrm{h})^{-1}$, and the latter receiving 38–64 mm $(3\,\mathrm{h})^{-1}$. In addition, much of the strongest upslope forcing in the dry members is downwind of at least one other band of upslope, meaning that some of the available moisture in the environment could have been precipitated out upstream. This setup would leave less moisture available for the upslope forcing toward the downstream

parts of the Catskills, reducing rainfall rates there. The bands of upslope are aligned differently in the wetter members, so that more of the available forcing for ascent is not downwind of any other upslope. All of this evidence supports the first hypothesis, which stated that wetter members feature greater overall upslope forcing over the Catskills.

The second hypothesis was tested by comparing the composite 100–1000-hPa layer mean winds, 100–1000-hPa integrated moisture transport by the southeasterly wind (which was the dominant direction of moisture transport for both clusters), and convergence of the 100–1000-hPa integrated moisture transport (including all wind directions) for the wetter, western cluster (Fig. 16a) and the drier, eastern cluster (Fig. 16b), at the time of maximum

a) Wetter, Western Cluster Schematic   b) Drier, Eastern Cluster Schematic
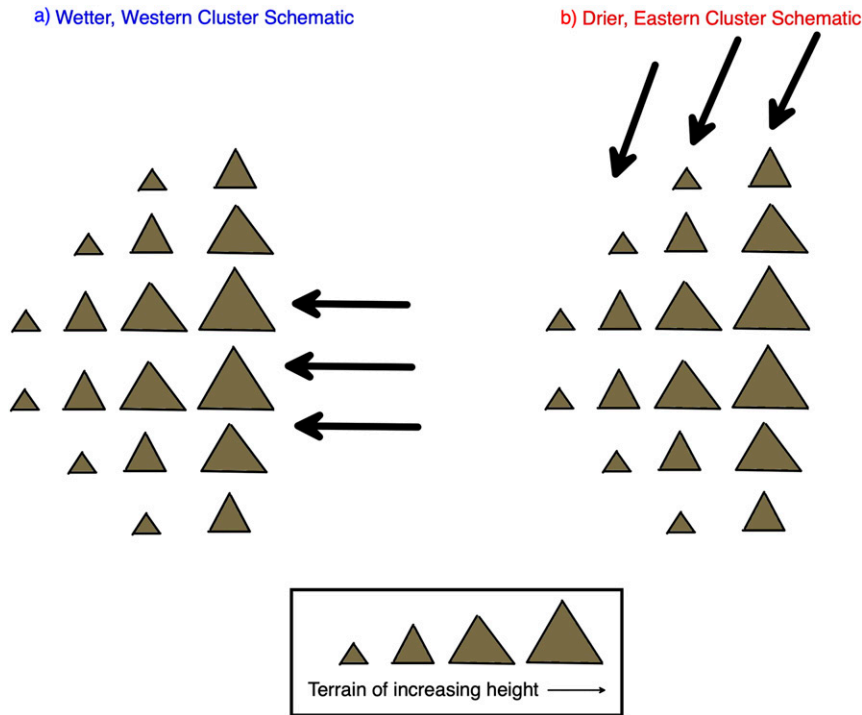

FIG. 14. Schematic of the relationship between the 39-h 900-hPa prevailing wind direction (shown as arrows), and topography (shown as triangles) for (a) the wet, western cluster and (b) the dry, eastern cluster.

precipitation over the Catskills. Not only do wetter members have greater moisture transport by the south-easterly wind into the Catskills (as can be seen by the larger contour values in Fig. 16a), they also have greater moisture convergence over the mountain range (with a maximum of $60 \times 10^{-4}\,\mathrm{kg\,m^{-2}\,s^{-1}}$, as opposed to a maximum of $30 \times 10^{-4}\,\mathrm{kg\,m^{-2}\,s^{-1}}$ in the drier members), which would be associated with increased precipitation.
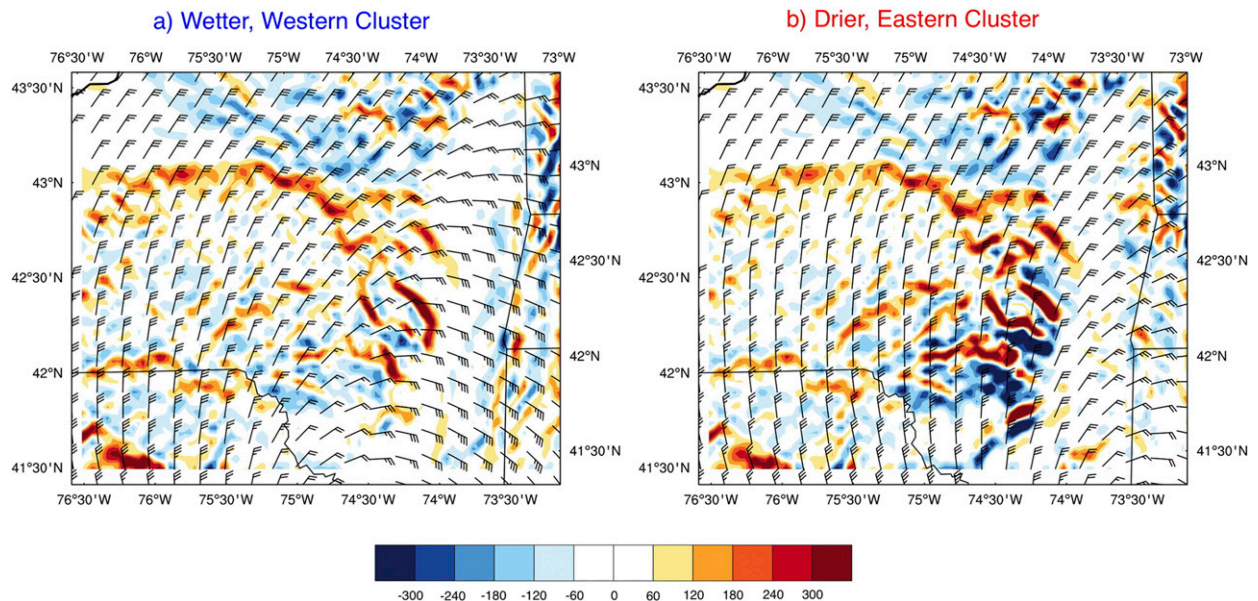
FIG. 15. The 39-h surface upslope velocity (shaded; $1 \times 10^{-3}\,\mathrm{m\,s^{-1}}$) and 900-hPa winds (barbs; $\mathrm{m\,s^{-1}}$) for (a) the wet, western cluster and (b) the dry, eastern cluster.
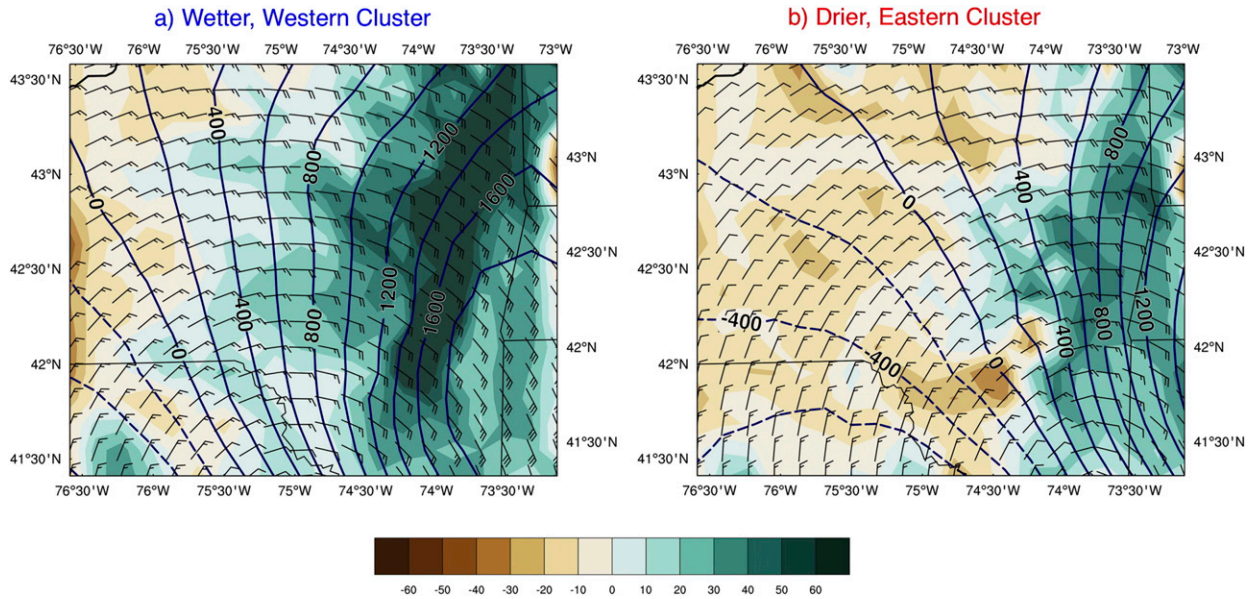
FIG. 16. The 39-h 100–1000-hPa layer mean winds (barbs; m s^{-1}), integrated moisture transport by the southeasterly wind (contours; every 200 kg m^{-1} s^{-1}), and integrated moisture transport convergence (shaded; 1×10^{-4} kg m^{-2} s^{-1}) for the (a) wet, western cluster and (b) dry, eastern cluster.

By contrast, the drier members shift the bulk of the moisture flux convergence farther east, and place moisture divergence over the Catskills (shown by the brown shading in southeastern New York). The divergence is especially strong over the southeast part of the Catskills, where the drier members have a region of strong downslope forcing. This evidence supports the second hypothesis, which stated that wetter members have

increased moisture flux convergence over the Catskills. It should be noted again, however, that the first two hypotheses are not independent of one another, as upslope forcing is often associated with moisture convergence.

Finally, the third hypothesis is tested by comparing the composite 500–800-hPa layer mean **Q** vectors and isotherms, and the **Q**-vector convergence for the wetter cluster (Fig. 17a) and the drier cluster (Fig. 17b), at the

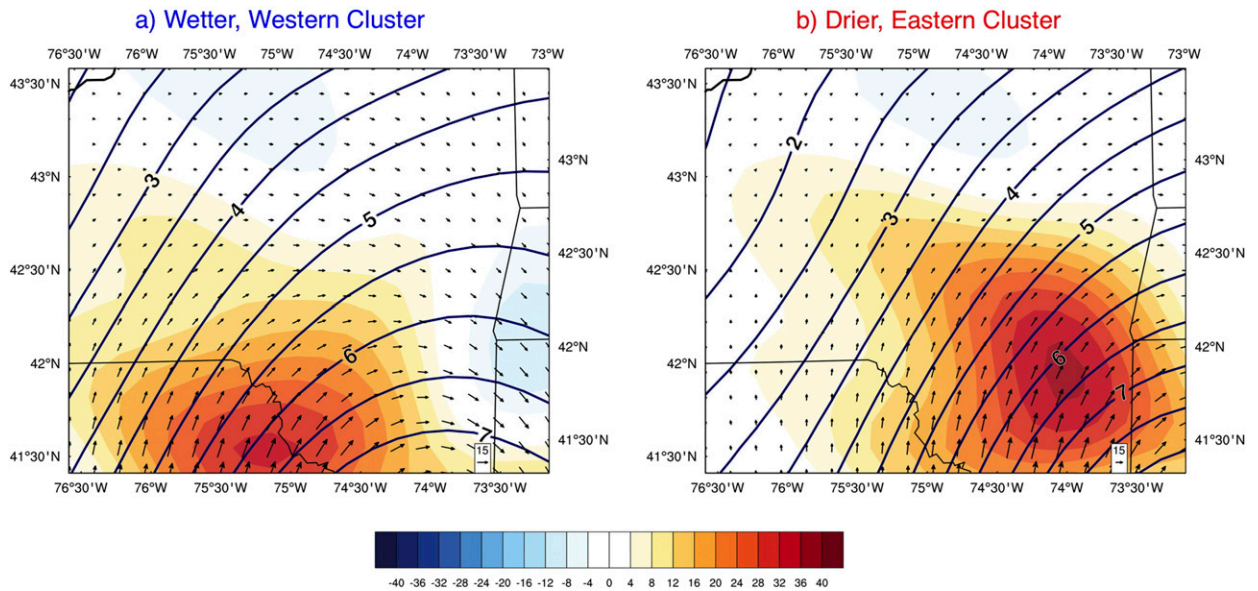FIG. 17. The 39-h 500–800-hPa layer mean **Q** vectors (arrows; 1×10^{-12} m^2 kg^{-1} s^{-1}), isotherms (contoured; every 0.5 K), and **Q**-vector convergence (shaded; 1×10^{-17} m kg^{-1} s^{-1}) for (a) the wet, western cluster and (b) the dry, eastern cluster.
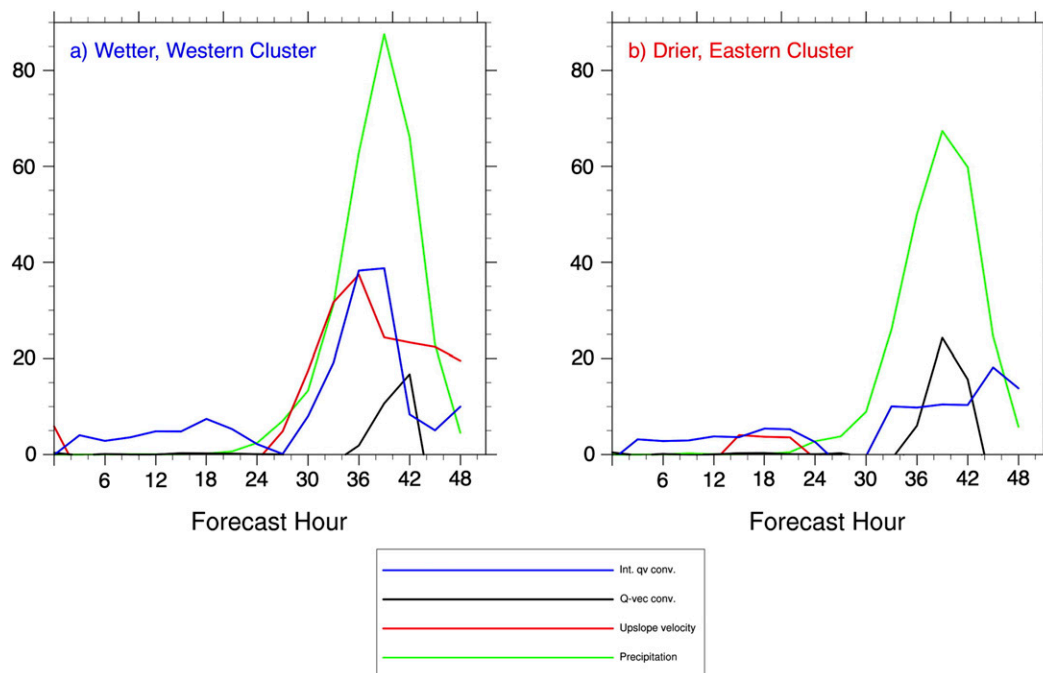
FIG. 18. Scaled time series of Catskills upslope (red; 1×10^{-3} m s^{-1}) and moisture convergence (blue; 1×10^{-4} kg m^{-2} s^{-1}) over Catskills locations that received the top 20th percentile of precipitation accumulations, as well as $\mathbf{Q}$-vector convergence (black; 1×10^{-17} m kg^{-1} s^{-1}) and precipitation [green; mm (3 h)$^{-1}$] over the domain 41.75°–42.75°N, 73.9°–75.25°W.

time of maximum precipitation over the Catskills. The 500–800-hPa layer was selected because it represented the layer of strongest forcing for ascent. Convergence of **Q** vectors indicates quasigeostrophic forcing for ascent (Hoskins and Pedder 1980), so if the wetter members position the region of maximum **Q**-vector convergence over the Catskills, it could enhance rainfall in that region. The **Q** vectors are defined as

$$\mathbf{Q} = \left[-\frac{R}{p}\left(\frac{\partial u_g}{\partial x}\frac{\partial T}{\partial x} + \frac{\partial v_g}{\partial x}\frac{\partial T}{\partial y} \right), -\frac{R}{p}\left(\frac{\partial u_g}{\partial y}\frac{\partial T}{\partial x} + \frac{\partial v_g}{\partial y}\frac{\partial T}{\partial y} \right) \right],$$

where **Q** is the total **Q** vector, u_g and v_g are the zonal and meridional components of the geostrophic wind, and $-(R/p)(\partial T/\partial x)$ and $-(R/p)(\partial T/\partial y)$ are the zonal and meridional gradients of potential temperature (R is the ideal gas constant for dry air, p is pressure, and T is temperature; Sanders and Hoskins 1990).

Surprisingly, Fig. 17 shows that the drier, eastern members actually feature stronger **Q**-vector convergence (and, therefore, quasigeostrophic forcing for ascent) than the wetter members (40×10^{-17} m kg^{-1} s^{-1} of convergence in the dry members, as opposed to around 20×10^{-17} m kg^{-1} s^{-1} of convergence in the wet members). Therefore, it appears that differences in synoptic forcing do not explain the differences in rainfall between

the wet and dry members. The drier members have much stronger synoptic forcing for ascent and, thus, for precipitation, at this time interval, despite their lower rainfall totals.

One way to compare the main drivers for precipitation in the wetter and drier clusters is to compare composite time series of all the metrics discussed in this section (precipitation, upslope, moisture convergence, and quasigeostrophic forcing; Fig. 18). The synoptic-scale metrics (precipitation and quasigeostrophic forcing) are area-averaged over the entire Catskills domain, while the mesoscale metrics (upslope and moisture convergence) are area-averaged only over the grid points in the domain that received the top 20th percentile of precipitation values (where they were relevant to the production of Catskills precipitation). The wetter members feature large upslope (in red) and moisture convergence (in blue) values from around 24 h into the forecast (when precipitation began over the Catskills) to the end of the model run, with peaks at 36 and 39 h, which correspond with the interval of maximum precipitation over the region (Fig. 18a). The drier members have some weak upslope forcing initially, but this does not last, while moisture convergence values remain moderate throughout the duration of the model run (Fig. 18b). By contrast, the dry members' precipitation

curve (in green) closely follows the shape of the **Q**-vector convergence curve (in black), with both peaking at 39 h and then decreasing to the end of the model run.

6. Summary and conclusions

As TCs move into the midlatitudes, they are often associated with heavy precipitation and devastating floods, such as occurred with Hurricane Irene (2011) over the Northeast. The goal of this work was to understand the synoptic and mesoscale dynamics that modulated precipitation forecasts over the Catskill region of New York during Hurricane Irene by examining global and regional ensemble forecasts initialized 36 h before Irene made landfall. In particular, the goal was to determine why some ensemble members predicted large precipitation totals over the Catskills, while others predicted much less.

A large amount of variability existed in an 80-member GFS ensemble in terms of precipitation in the Catskills. The differences that existed between the 10 members with the most forecast precipitation and the 10 members with the least were almost entirely due to the forecast position of Irene. In the wetter members, Irene tracked farther to the west, while the drier members featured a more eastward path. For this set of forecasts, differences in storm motion appear to originate with the PV initialized to the southwest of Irene, such that the wetter members were characterized by greater cyclonic PV in a tropopause-based trough to the southwest of the storm center, which placed the hurricane in a region of anomalous easterly steering flow. This steering flow started Irene on a more westward track, enabling its upper-level outflow to deform an approaching trough. With the trough remaining well upstream, Irene was able to track farther to the west, positioning the region of maximum rainfall directly over eastern New York and southern Vermont. These results imply that the variability in forecast precipitation distribution between ensemble members was largely controlled by storm position.

The 0.5° GFS output was then used as boundary conditions for a 3-km WRF nest, in order to allow a better representation of mesoscale processes and the effects of terrain on the precipitation distribution. Contrary to the GFS-based results, the 3-km WRF output does not show a linear relationship between storm track and precipitation over the Catskills. Instead, precipitation in the wetter members was driven primarily by mesoscale processes related to terrain effects (strong upslope forcing and moisture convergence), while precipitation in the drier members was driven primarily by quasigeostrophic forcing for ascent. The wetter members featured easterly low-level flow directly into the sharp terrain gradient of the eastern Catskills, creating large upslope magnitudes, while the drier members had more northerly low-level flow, which resulted in less upslope. Likewise, the wetter members were characterized by stronger moisture transport into the region than the drier members and greater convergence of that moisture (the larger upslope magnitudes likely contributed to this convergence). The drier members, on the other hand, had stronger **Q**-vector convergence than the wetter members and, therefore, greater quasigeostrophic forcing for ascent. All of this illustrates the dominance of terrain and mesoscale processes in producing large rainfall totals, as the members with a favorable upslope and moisture convergence setup were able to produce substantially more precipitation than the quasigeostophically forced cluster.

As seen with these results, TC-related rainfall totals can be dependent on a complex interaction between storm motion and relative location with respect to topography. The worst flooding can result when a storm's low-level winds are perpendicular to a steep terrain gradient in an already moist environment and the enhanced precipitation over that terrain can later overwhelm downstream watersheds. A small difference in storm track can result in large variability in precipitation rate. Clustering ensemble members into specific forecast scenarios can reveal more information when forecasting such events than just using the ensemble mean and standard deviation, as it allows forecasters to evaluate several possible forecasts that appear in an ensemble. The addition of this technique to a TC forecaster's repertoire has the potential to improve the accuracy of hurricane impact forecasts.

REFERENCES

Archambault, H. M., L. F. Bosart, D. Keyser, C. A. Davis, and J. M. Cordeira, 2015: A composite perspective of the extratropical flow response to recurving western North Pacific tropical cyclones. *Mon. Wea. Rev.*, **143**, 1122–1141, https://doi.org/10.1175/MWR-D-14-00270.1.

Atallah, E. H., and L. F. Bosart, 2003: The extratropical transition and precipitation distribution of Hurricane Floyd (1999).

Mon. Wea. Rev., **131**, 1063–1081, https://doi.org/10.1175/1520-0493(2003)131<1063:TETAPD>2.0.CO;2.

——, ——, and A. R. Aiyyer, 2007: Precipitation distribution associated with landfalling tropical cyclones over the eastern United States. *Mon. Wea. Rev.*, **135**, 2185–2206, https://doi.org/10.1175/MWR3382.1.

Avila, L. A., and J. P. Cangialosi, 2011: Tropical Cyclone Report: Hurricane Irene. National Hurricane Center Tropical Cyclone, Tech. Rep. AL092011, 45 pp.

Bassill, N. P., 2015: An analysis of the operational GFS simplified Arakawa Schubert parameterization within a WRF framework: A Hurricane Sandy (2012) long-term track forecast perspective. *J. Geophys. Res. Atmos.*, **120**, 378–398, https://doi.org/10.1002/2014JD022211.

Benjamin, S. G., and Coauthors, 2004: An hourly assimilation–forecast cycle: The RUC. *Mon. Wea. Rev.*, **132**, 495–518, https://doi.org/10.1175/1520-0493(2004)132<0495:AHACTR>2.0.CO;2.

——, and Coauthors, 2016: A North American hourly assimilation and model forecast cycle: The Rapid Refresh. *Mon. Wea. Rev.*, **144**, 1669–1694, https://doi.org/10.1175/MWR-D-15-0242.1.

Bosart, L. F., and D. B. Dean, 1991: The Agnes rainstorm of June 1972—Surface-feature evolution culminating in inland storm redevelopment. *Wea. Forecasting*, **6**, 515–537, https://doi.org/10.1175/1520-0434(1991)006<0515:TAROJS>2.0.CO;2.

Carpenter, R. L., and Coauthors, 2004: A globally relocatable numerical weather prediction system based on WRF and ADAS. *20th Conf. on Weather Analysis and Forecasting/16th Conf. on Numerical Weather Prediction*, Seattle, WA, Amer. Meteor. Soc., 14.3, https://ams.confex.com/ams/84Annual/techprogram/paper_73106.htm.

Carr, L. E., and R. L. Elsberry, 2000: Dynamical tropical cyclone track forecast errors. Part II: Midlatitude circulation influences. *Wea. Forecasting*, **15**, 662–681, https://doi.org/10.1175/1520-0434(2000)015<0662:DTCTFE>2.0.CO;2.

Chen, L. S., Y. Li, and Z. Q. Cheng, 2010: An overview of research and forecasting on rainfall associated with landfalling tropical cyclones. *Adv. Atmos. Sci.*, **27**, 967–976, https://doi.org/10.1007/s00376-010-8171-y.

Colle, B. A., 2003: Numerical simulations of the extratropical transition of Floyd (1999): Structural evolution and responsible mechanisms for the heavy rainfall over the Northeast United States. *Mon. Wea. Rev.*, **131**, 2905–2926, https://doi.org/10.1175/1520-0493(2003)131<2905:NSOTET>2.0.CO;2.

Davis, C. A., 1992: Piecewise potential vorticity inversion. *J. Atmos. Sci.*, **49**, 1397–1411, https://doi.org/10.1175/1520-0469(1992)049<1397:PPVI>2.0.CO;2.

——, S. C. Jones, and M. Riemer, 2008: Hurricane vortex dynamics during Atlantic extratropical transition. *J. Atmos. Sci.*, **65**, 714–736, https://doi.org/10.1175/2007JAS2488.1.

——, D. A. Ahijevych, W. Wang, and W. C. Skamarock, 2016: Evaluating medium-range tropical cyclone forecasts in uniform- and variable-resolution global models. *Mon. Wea. Rev.*, **144**, 4141–4160, https://doi.org/10.1175/MWR-D-16-0021.1.

DiMego, G. J., and L. F. Bosart, 1982: The transformation of tropical storm Agnes into an extratropical cyclone. Part I: The observed fields and vertical motion computations. *Mon. Wea. Rev.*, **110**, 385–411, https://doi.org/10.1175/1520-0493(1982)110<0385:TTOTSA>2.0.CO;2.

Du, J., 2011: GCIP/EOP surface: Precipitation NCEP/EMC 4KM Gridded Data (GRIB) Stage IV data, version 1.0. UCAR/NCAR–Earth Observing Laboratory, accessed 1 August 2018, https://doi.org/10.5065/D6PG1QDD.

Eckhardt, S., A. Stohl, H. Wernli, P. James, C. Forster, and N. Spichtinger, 2004: A 15-year climatology of warm conveyor belts. *J. Climate*, **17**, 218–237, https://doi.org/10.1175/1520-0442(2004)017<0218:AYCOWC>2.0.CO;2.

Epstein, E. S., 1969: A scoring system for probability forecasts of ranked categories. *J. Appl. Meteor.*, **8**, 985–987, https://doi.org/10.1175/1520-0450(1969)008<0985:ASSFPF>2.0.CO;2.

Evans, C., and Coauthors, 2017: The extratropical transition of tropical cyclones. Part I: Cyclone evolution and direct impacts. *Mon. Wea. Rev.*, **145**, 4317–4344, https://doi.org/10.1175/MWR-D-17-0027.1.

Galarneau, T. J., and C. A. Davis, 2013: Diagnosing forecast errors in tropical cyclone motion. *Mon. Wea. Rev.*, **141**, 405–430, https://doi.org/10.1175/MWR-D-12-00071.1.

Gao, S., Z. Meng, F. Zhang, and L. F. Bosart, 2009: Observational analysis of heavy rainfall mechanisms associated with severe Tropical Storm Bilis (2006) after its landfall. *Mon. Wea. Rev.*, **137**, 1881–1897, https://doi.org/10.1175/2008MWR2669.1.

Gleeson, T. A., 1970: Statistical-dynamical predictions. *J. Appl. Meteor.*, **9**, 333–344, https://doi.org/10.1175/1520-0450(1970)009<0333:SDP>2.0.CO;2.

Harr, P. A., and R. L. Elsberry, 1996: Structure of a mesoscale convective system embedded in Typhoon Robyn during TCM-93. *Mon. Wea. Rev.*, **124**, 634–652, https://doi.org/10.1175/1520-0493(1996)124<0634:SOAMCS>2.0.CO;2.

——, D. Anwender, and S. C. Jones, 2008: Predictability associated with the downstream impacts of the extratropical transition of tropical cyclones: Methodology and a case study of Typhoon Nabi (2005). *Mon. Wea. Rev.*, **136**, 3205–3225, https://doi.org/10.1175/2008MWR2248.1.

Hart, R. E., and J. L. Evans, 2001: A climatology of the extratropical transition of Atlantic tropical cyclones. *J. Climate*, **14**, 546–564, https://doi.org/10.1175/1520-0442(2001)014<0546:ACOTET>2.0.CO;2.

Hartigan, J. A., and M. A. Wong, 1979: Algorithm AS 136: A K-means clustering algorithm. *J. Roy. Stat. Soc. Ser. C Appl. Stat.*, **28**, 100–108, https://doi.org/10.2307/2346830.

Hoskins, B. J., and M. A. Pedder, 1980: The diagnosis of middle latitude synoptic development. *Quart. J. Roy. Meteor. Soc.*, **106**, 707–719, https://doi.org/10.1002/qj.49710645004.

——, M. E. McIntyre, and A. W. Robertson, 1985: On the use and significance of isentropic potential vorticity maps. *Quart. J. Roy. Meteor. Soc.*, **111**, 877–946, https://doi.org/10.1002/qj.49711147002.

Jones, S. C., and Coauthors, 2003: The extratropical transition of tropical cyclones: Forecast challenges, current understanding, and future directions. *Wea. Forecasting*, **18**, 1052–1092, https://doi.org/10.1175/1520-0434(2003)018<1052:TETOTC>2.0.CO;2.

Kain, J. S., 2004: The Kain–Fritsch convective parameterization: An update. *J. Appl. Meteor.*, **43**, 170–181, https://doi.org/10.1175/1520-0450(2004)043<0170:TKCPAU>2.0.CO;2.

Karstens, C. D., and Coauthors, 2015: Evaluation of a probabilistic forecasting methodology for severe convective weather in the 2014 Hazardous Weather Testbed. *Wea. Forecasting*, **30**, 1551–1570, https://doi.org/10.1175/WAF-D-14-00163.1.

Keller, J. H., and Coauthors, 2019: The extratropical transition of tropical cyclones. Part II: Interaction with the midlatitude flow, downstream impacts, and implications for predictability. *Mon. Wea. Rev.*, **147**, 1077–1106, https://doi.org/10.1175/MWR-D-17-0329.1.

Klein, P. M., P. A. Harr, and R. L. Elsberry, 2000: Extratropical transition of western North Pacific tropical cyclones: An overview and conceptual model of the transformation stage.

Wea. Forecasting, **15**, 373–395, https://doi.org/10.1175/1520-0434(2000)015<0373:ETOWNP>2.0.CO;2.

Krishnamurti, T. N., 1995: Numerical weather prediction. *Annu. Rev. Fluid. Mech.*, **27**, 195–225, https://doi.org/10.1146/annurev.fl.27.010195.001211.

——, C. M. Kishtawal, Z. Zhang, T. Larow, D. Bachiochi, and E. Williford, 2000: Multimodel ensemble forecasts for weather and seasonal climate. *J. Climate*, **13**, 4196–4216, https://doi.org/10.1175/1520-0442(2000)013<4196:MEFFWA>2.0.CO;2.

Landsea, C. W., and J. L. Franklin, 2013: Atlantic hurricane database uncertainty and presentation of a new database format. *Mon. Wea. Rev.*, **141**, 3576–3592, https://doi.org/10.1175/MWR-D-12-00254.1.

Lin, C. Y., H. M. Hsu, Y. F. Shengl, C. H. Kuo, and Y. A. Liou, 2011: Mesoscale processes for super heavy rainfall of Typhoon Morakot (2009) over southern Taiwan. *Atmos. Chem. Phys.*, **11**, 345–361, https://doi.org/10.5194/acp-11-345-2011.

Lin, Y.-L., S. Chiao, T.-A. Wang, M. L. Kaplan, and R. P. Weglarz, 2001: Some common ingredients for heavy orographic rainfall. *Wea. Forecasting*, **16**, 633–660, https://doi.org/10.1175/1520-0434(2001)016<0633:SCIFHO>2.0.CO;2.

Lorenz, E. N., 1963: Deterministic nonperiodic flow. *J. Atmos. Sci.*, **20**, 130–141, https://doi.org/10.1175/1520-0469(1963)020<0130:DNF>2.0.CO;2.

Michalakes, J., S. Chen, J. Dudhia, L. Hart, J. Klemp, J. Middlecoff, and W. Skamarock, 2001: Development of a next-generation regional weather research and forecasting model. *Developments in Teracomputing: Proceedings Ninth ECMWF Workshop on the Use Of High Performance Computing in Meteorology*, W. Zwieflhofer and N. Kreitz, Eds., World Scientific, 269–276.

Mlawer, E. J., S. J. Taubman, P. D. Brown, M. J. Iacono, and S. A. Clough, 1997: Radiative transfer for inhomogeneous atmospheres: RRTM, a validated correlated-k model for the longwave. *J. Geophys. Res.*, **102**, 16 663–16 682, https://doi.org/10.1029/97JD00237.

Nakanishi, M., and H. Niino, 2009: Development of an improved turbulence closure model for the atmospheric boundary layer. *J. Meteor. Soc. Japan*, **87**, 895–912, https://doi.org/10.2151/jmsj.87.895.

Rabier, F., 2005: Overview of global data assimilation developments in numerical weather-prediction centres. *Quart. J. Roy. Meteor. Soc.*, **131**, 3215–3233, https://doi.org/10.1256/qj.05.129.

Riemer, M., S. C. Jones, and C. A. Davis, 2008: The impact of extratropical transition on the downstream flow: An idealized modelling study with a straight jet. *Quart. J. Roy. Meteor. Soc.*, **134**, 69–91, https://doi.org/10.1002/qj.189.

Ruxton, G. D., 2006: The unequal variance t-test is an underused alternative to Student's t-test and the Mann-Whitney U test. *Behav. Ecol.*, **17**, 688–690, https://doi.org/10.1093/beheco/ark016.

Sanders, F., and B. J. Hoskins, 1990: An easy method for estimation of Q-vectors from weather maps. *Wea. Forecasting*, **5**, 346–353, https://doi.org/10.1175/1520-0434(1990)005%3C0346:AEMFEO%3E2.0.CO;2.

Tang, B., M. Vaughan, R. Lazear, K. Corbosiero, L. Bosart, T. Wasula, I. Lee, and K. Lipton, 2016: Topographic and boundary influences on the 22 May 2014 Duanesburg, New York, tornadic supercell. *Wea. Forecasting*, **31**, 107–127, https://doi.org/10.1175/WAF-D-15-0101.1.

Thompson, G., R. M. Rasmussen, and K. Manning, 2004: Explicit forecasts of winter precipitation using an improved bulk microphysics scheme. Part I: Description and sensitivity analysis. *Mon. Wea. Rev.*, **132**, 519–542, https://doi.org/10.1175/1520-0493(2004)132%3C0519:EFOWPU%3E2.0.CO;2.

Torn, R. D., J. S. Whitaker, P. Pegion, T. M. Hamill, and G. J. Hakim, 2015: Diagnosis of the source of GFS medium-range track errors in Hurricane Sandy (2012). *Mon. Wea. Rev.*, **143**, 132–152, https://doi.org/10.1175/MWR-D-14-00086.1.

——, T. J. Elless, P. P. Papin, and C. A. Davis, 2018: Tropical cyclone track sensitivity in deformation steering flow. *Mon. Wea. Rev.*, **146**, 3183–3201, https://doi.org/10.1175/MWR-D-18-0153.1.

Whitaker, J. S., and T. M. Hamill, 2002: Ensemble data assimilation without perturbed observations. *Mon. Wea. Rev.*, **130**, 1913–1924, https://doi.org/10.1175/1520-0493(2002)130<1913:EDAWPO>2.0.CO;2.

Wu, C. C., and Y. H. Kuo, 1999: Typhoons affecting Taiwan: Current understanding and future challenges. *Bull. Amer. Meteor. Soc.*, **80**, 67–80, https://doi.org/10.1175/1520-0477(1999)080<0067:TATCUA>2.0.CO;2.

——, T.-H. Yen, Y.-H. Kuo, and W. Wang, 2002: Rainfall simulation associated with Typhoon Herb (1996) near Taiwan. Part I: The topographic effect. *Wea. Forecasting*, **17**, 1001–1015, https://doi.org/10.1175/1520-0434(2003)017<1001:RSAWTH>2.0.CO;2.

——, J.-H. Chen, P.-H. Lin, and K.-H. Chou, 2007: Targeted observations of tropical cyclone movement based on the adjoint-derived sensitivity steering vector. *J. Atmos. Sci.*, **64**, 2611–2626, https://doi.org/10.1175/JAS3974.1.

Yamaguchi, M., F. Vitart, S. T. K. Lang, L. Magnusson, R. L. Elsberry, G. Elliott, M. Kyouda, and T. Nakazawa, 2015: Global distribution of the skill of tropical cyclone activity forecasts on short- to medium-range time scales. *Wea. Forecasting*, **30**, 1695–1709, https://doi.org/10.1175/WAF-D-14-00136.1.